

# Variability of Galactic blue supergiants observed with TESS

Michalis Kourniotis<sup>1\*</sup>, Lydia S. Cidale<sup>2,3</sup>, Michaela Kraus<sup>1</sup>, Matias A. Ruiz Diaz<sup>2,3</sup>, and Aldana Alberici Adam<sup>2,3</sup>

<sup>1</sup> Astronomical Institute, Czech Academy of Sciences, Fričova 298, 251 65 Ondřejov, Czech Republic

<sup>2</sup> Instituto de Astrofísica La Plata, CCT La Plata, CONICET-UNLP, Paseo del Bosque S/N, B1900FWA, La Plata, Argentina

<sup>3</sup> Departamento de Espectroscopía, Facultad de Ciencias Astronómicas y Geofísicas, Universidad Nacional de La Plata (UNLP), Paseo del Bosque S/N, B1900FWA, La Plata, Argentina

Received 24/09/2024; accepted 26/03/2025

## ABSTRACT

**Context.** Blue supergiants (BSGs) mediate between the main sequence and the late stages of massive stars, which makes them valuable for assessing the physics that drives the stars across the diverse evolutionary channels.

**Aims.** By exploring correlations between the parameters of BSGs and their variability properties, we aim to improve the constraints on the models of the evolved star structure and on the physics of the post-main-sequence evolution.

**Methods.** We conducted a variability study of 41 BSGs with known spectroscopic parameters in the Galaxy using high-precision photometry from the Transiting Exoplanet Survey Satellite. Stellar luminosities were calculated from the fit of multiband photometry and using the latest distance estimates from *Gaia*. We described the time domain of the stars by means of three statistical measures and extracted prominent frequencies via an iterative pre-whitening process. Alongside, we investigated the debated stochastic low-frequency (SLF) variability, which manifests itself in all amplitude spectra.

**Results.** We report a positive correlation between the amplitude of photometric variability and the stellar luminosity. For  $\log(L/L_{\odot}) \leq 5$ , stars display frequencies that match the rotational one, suggesting that variability is presumably driven by surface spots and/or features embedded in the wind. For  $\log(L/L_{\odot}) \geq 5$ , variables of the  $\alpha$  Cygni class manifest themselves with their diverse and/or time-variant photometric properties and their systematically lower frequencies. Moreover, we report a positive correlation between the SLF variability amplitude and the effective temperature, indicating an influential role that the stellar age plays on the emergence of the background signal beyond the main sequence. Positive, though weak, correlation is also observed between the intrinsic brightness and the SLF variability amplitude, similar to the findings in the Large Magellanic Cloud, which suggests an in common excitation mechanism that depends only mildly on metallicity. Exceptionally, the  $\alpha$  Cygni variables display a suppressed SLF variability that prompts to the interior changes that the evolving stars undergo.

**Key words.** stars: massive – stars: variables: general – stars: rotation – stars: oscillations – stars: evolution

## 1. Introduction

Being among the brightest stars in galaxies and young star associations, the blue supergiants (BSGs) are messengers of information on key parameters of their host environment such as age, kinematics, metallicity, and distance (Bresolin et al. 2006; Urbaneja et al. 2008; Kudritzki et al. 2012). Their accessibility enables studies to be undertaken with high resolution, and on a systematic basis, providing the means to describe mechanisms that are pivotal to the evolution of massive stars.

The high number of reported BSGs (Castro et al. 2014; de Burgos et al. 2023) contradicts the scarcity predicted by the standard single-star evolutionary theory (Bellinger et al. 2024), which is referred to as the BSG problem. To resolve this discrepancy, several scenarios to create BSGs in addition to the classical post-main sequence objects have been proposed. Namely being stars that experience an extended main-sequence phase due to possessing enlarged convective cores (Brott et al. 2011; Martinet et al. 2021) or due to displaying enhanced rotationally-induced mixing (de Mink et al. 2013), post-mass-transfer stars (Farrell et al. 2019), stripped-envelope stars (Klencki et al. 2022), and binary mergers (Henneco et al. 2024; Menon et al. 2024). In this respect, key to assessing the nature of BSGs and to interpret-

ing their statistics is the thorough understanding of their interior, mass loss, and of their interplay between binary components.

Further contributing to the puzzling demographics of BSGs, several members of the class are believed to have already passed through the phase of red supergiants (RSGs) and are now captured at late stages (Meynet et al. 2015). These, so-called post-RSGs, have experienced significant loss of their hydrogen envelope, exposing products from the interior to the surface and surroundings. Spectroscopic tracers of this processed material provide means to identify the evolved status of several of these objects (e.g. Kraus et al. 2023), although other post-RSGs cease to show abnormal chemistry (Georgy et al. 2014) or a gaseous/dusty circumstellar environment (Oudmaijer et al. 2009). The interior of post-RSGs is subject to non-adiabatic processes (Saio et al. 2013; Glatzel & Kraus 2024), which are linked to the yet poorly-understood strange-mode instabilities. These have been proposed to be responsible for the launch of episodic mass loss and might lead to a build-up of circumstellar envelopes (Aerts et al. 2010). They also require that the stars have experienced copious amounts of mass loss in a short time, during their prior RSG phase (Saio et al. 2013; Georgy et al. 2014; Glatzel & Kraus 2024). Moreover, post-RSG BSGs display semi-regular variability and periods of few to several tens of days, which are attributed to opacity-driven oscillations (Kaufman et al. 1997;

\* email: kourniotis@asu.cas.cz

Lefever et al. 2007). These objects are known as  $\alpha$  Cygni variables, following the name of the prototype BSG star.

The stellar variability integrates the feedback from the different processes that take place in the interior and atmosphere, serving as a potent indicator of the structural changes that stars undergo at different stages of evolution. From the interior of BSGs, the most commonly studied sources of (quasi-)periodic and stochastic signal include p-/g-modes that are driven by the  $\kappa$ -mechanism operating in the metal opacity bump (e.g. Saio et al. 2006; Lefever et al. 2007), low-frequency waves that are generated by sub-photospheric convection (Cantiello et al. 2009), and internal gravity waves (IGWs; Bowman et al. 2019b, 2020). As soon as the waves reach the surface, they manifest as coherent or stochastic fluctuations in the brightness and variability in the line profiles (e.g. Kaufer et al. 2006; Simón-Díaz et al. 2018). Moreover, pulsations are believed to contribute to line broadening through the effect of macroturbulence (Aerts et al. 2009; Simón-Díaz et al. 2010; Aerts et al. 2018; Bowman et al. 2020). Beyond the interior, rotational modulation is another source of periodic signal that is generated by spots in the surface and/or co-rotating inhomogeneities in the wind (Aerts et al. 2013, 2018). Evidence of the deep interior dynamics propagating into the wind has been demonstrated (Kraus et al. 2015; Haucke et al. 2018; Aerts et al. 2017; Cidale et al. 2023), implying an auxiliary role of the pulsations in contributing to the line-driven mass loss. Finally, stellar encounters introduce variability in the case of eclipsing and/or spectroscopic systems, and via indication in the frequency spectra of mixed or tidally-induced modes (Degroote et al. 2012; Southworth et al. 2020).

Probably the most debated type of variability in the frequency spectra of early-type stars is the stochastic low-frequency (SLF) variability. Its first detection in three O-type stars by Blomme et al. (2011) has been followed by systematic analyses over extended OB-star samples that confirmed the ubiquity of the signal (Bowman et al. 2019a,b, 2020; Burssens et al. 2020; Ma et al. 2024; Shen et al. 2024). Hydrodynamical simulations of core convection and wave propagation have been able to reproduce the observed SLF variability, assigning its origin to IGWs that are excited at the interface between the convective core and the radiative envelope (Rogers et al. 2013; Edelman et al. 2019; Ratnasingam et al. 2023). Other studies, on the other hand, have demonstrated that core-excited IGWs are unlikely to generate variability consistent to the observations (Lecoanet et al. 2019; Anders et al. 2023); a thoroughly discussed alternative to the core-convection scenario is the turbulent motion in the sub-surface convection zones of the stellar envelope (Cantiello et al. 2021; Schultz et al. 2022). The latter excitation mechanism alone, however, is believed to be unfavorable for stars at low-metallicity environments where this form of variability is observed to persist (Bowman et al. 2024), as well as for stars in the main sequence that presumably lack sub-surface convection zones (e.g. Jermyn et al. 2022). Recent findings suggest that both core and near-surface convection could shape the discussed signal over different ranges of frequencies in the power spectra of the stars (Thompson et al. 2024), whereas, the possibility that the inductive role of the two mechanisms relies upon the stellar age and metallicity is too under consideration (Bowman et al. 2024). As the discussion on the source of the enigmatic signal continues, refining the knowledge on its underlying physics has important implications for the modeling of stellar evolution, due to the role of the propagating waves in driving the angular momentum transport, rotation and mixing in the interior of the stars (Rogers et al. 2013; Aerts et al. 2019; Bowman 2020).

The signatures of the ambiguous processes that govern the nature of BSGs are imprinted into their variability profile. Applying advanced methodology for the exploration of the frequency domain is shown to be effective in identifying different oscillation modes, constraining parameters of the core, and even differentiating between the distinct evolutionary scenarios (Degroote et al. 2010; Bowman et al. 2019b; Bowman 2020; Burssens et al. 2023; Bellinger et al. 2024; Henneco et al. 2024). A particular breakthrough in asteroseismology has been achieved since the launch of NASA's Transiting Exoplanet Survey Satellite (TESS; Ricker et al. 2015). The mission holds a major advantage over its predecessor monitoring surveys thanks to its all-sky coverage, which enables systematic studies to be undertaken and statistical inferences to be drawn over stellar ensembles. The latter include massive stars at both early phases (e.g. Pedersen et al. 2019; Burssens et al. 2020; Krtićka & Feldmeier 2021; Gebruers et al. 2022; Labadie-Bartz et al. 2022) and at evolved (or transition) ones (Nazé et al. 2021; Dorn-Wallenstein et al. 2019, 2022; Spejcher et al. 2025). These works have been mapping the different manifestations as a function of the stellar parameters, collectively improving our understanding of the stellar structure and evolution. In the same line, we here present a variability study with TESS of southern Galactic BSGs, where we explore associations between their well-determined parameters and the features of the time and frequency domain. Particular attention is paid on the reported  $\alpha$  Cygni variables of the sample, probing for signatures of their evolved status on the variability statistics. Additionally, we model the SLF variability of the stars and compare its parameters to those from the study of BSGs in the Large Magellanic Cloud (LMC) (Bowman et al. 2019b). With the metallicity constrained, we aim to assist in narrowing down the scenarios on the ambiguous origin of the signal. The paper is organized as follows: in Sect. 2, we present the sample of the studied BSGs and the processing of their TESS data, in Sect. 3 we describe the process for extracting the frequencies from the multiperiodic signals and introduce the metrics for describing the time domain, and in Sect. 4, we proceed to fit the spectral energy distributions, which enables us to assess the stellar luminosities. We discuss the results of the study in Sect. 5, and provide concluding remarks in Sect. 6.

## 2. Sample selection and TESS photometry

### 2.1. Source catalog

Our explored sample is taken from the catalog of Fraser et al. (2010), which consists of Galactic B-type supergiants observed in 2004–2005 with the Fiber-fed Extended Range Optical Spectrograph (FEROS; Kaufer et al. 1999), a high-resolution spectrograph ( $R \sim 48\,000$ ) installed on the 2.2-m Max Planck Institute (MPI) telescope, at the European Southern Observatory (ESO), La Silla, Chile. The stellar parameters were extracted by fitting the observations with theoretical models, which were generated using the non-local thermodynamic equilibrium (non-LTE) code TLUSTY (Hubeny & Lanz 1995). The uncertainties in the  $\log g$  and  $\log T_{\text{eff}}$  measurements were reported as  $\pm 0.1$  dex and  $\pm 0.02$  dex, respectively.

### 2.2. TESS time-series data

Launched in 2018, TESS (Ricker et al. 2015) has been conducting monitoring of 85% of the sky with an angular resolution of  $21''/\text{pixel}$ , using a wide red/optical passband that spans the wavelength range 600 – 1 000 nm. The field-of-view of TESS covers

a sky area of  $24^\circ \times 96^\circ$  (known as sector), which is observed for two spacecraft orbits, or  $\sim 27$  days.

We performed cross-matching between the source catalog and the TESS database, removing stars that are not observed by TESS as well as those with poor-quality data (e.g. stars captured at the edge of the detector) that were unsuitable for further investigation. In addition, we excluded stars from the source catalog that are brighter than the TESS magnitude ( $T$ ) limit of 4 mag, a value that has been tested for the ability of the TESS CCD detectors to conserve charge from bright sources (Vanderspek et al. 2018). Our studied sample consists of 41 BSGs, which we present in Table A.1 of the Appendix, along with their coordinates and spectral classifications from Simbad, their TESS Input Catalog (TIC) number,  $T$ , and observed sectors.

For the systematic analysis of the time series data, we used the `lightkurve` software package (Lightkurve Collaboration et al. 2018). Two types of flux were explored; pre-processed and own extracted and systematics-corrected one.

### 2.2.1. PDCSAP flux

Using the `lightkurve.search_lightcurve` routine and the TIC identification number of the objects, we queried the Mikulski Archive for Space Telescopes<sup>1</sup> (MAST) for light curves that have been processed with the dedicated pipeline for the survey (Science Processing Operations Center; SPOC). The light curve files contain data that were taken with a 2-min cadence, and which have been corrected for the systematic trends using the co-trending Basis Vectors (CBVs) method (photometry flagged as PDCSAP\_FLUX; Pre-search Data Conditioning Simple Aperture Photometry). The provided data come along with the pixel mask (“optimal” aperture) that has been produced by the pipeline for the extraction of the photometric signal.

### 2.2.2. Full-frame images (FFIs)

As an adjunct to the study of the pre-processed flux, we explored cutouts from the full-frame images (FFIs), so-called target pixel files (TPFs), using the TESScut service (Brasseur et al. 2019). The process was performed with the `lightkurve.search_tesscut` routine and setting the cutout length to  $20 \times 20$  pixels, which was enough to encompass the entirety of the target flux and sufficient background signal, for all sample stars.

We superimposed photometric sources from the *Gaia* Data Release 3 (*Gaia* DR3; Gaia Collaboration 2022) database on the TPFs, and located the target star. We then overlaid the SPOC aperture and searched, sector by sector, for cases where adjustment of the aperture was desirable in order to minimize biases related to under-/overcollecting signal. In such an event, we defined a custom mask for manual extraction of the target flux; starting from the pixel containing the *Gaia* target source, we extended the aperture vertically (across the rows) in both directions of the charge blooming, for as long as the ratio of the flux to that of the target pixel remained higher than a threshold value. The process was repeated sideways for the adjacent columns. The threshold was evaluated empirically to include adequate signal of the studied star without excess contribution from the background; it was set to 0.15 for most of the sample stars, and reached down to 0.07. For three stars

proximal to a bright source (see Sect. 2.2.3), we increased this value up to 0.25. Next, the extracted light curves were corrected against the instrumental noise and the systematics using the `lightkurve.ReggressionCorrector` class. For this process, we defined as background pixels those fainter than a modest threshold ( $10^{-4}\sigma$ ) below the median flux of the TPF. The dimensionality of the background vector space was reduced using principal component analysis, and linear regression was performed to detrend the science data.

The processed data of each above types of fluxes were fit with a low-order polynomial and were detrended. We converted the normalized flux  $F_n$  to magnitudes using the formula

$$\Delta m = -2.5 \log_{10}(F_n) \quad (1)$$

The time series of consecutive sectors with the same cadence were then joined into a larger observing window in order to increase the resolution of our frequency analysis and accuracy of time-domain statistics. We display the light curves of selected BSGs in Fig. 1, and those of the entire sample in the Appendix B.

### 2.2.3. Contamination in the TESS aperture

The main drawback of TESS is the low spatial resolution, which makes densely populated areas in the sky prone to contamination effects. The degree of contamination for a TESS source can be assessed from the ratio of the light that comes from the target to the total light that is captured within the aperture. This metric is calculated by SPOC and is stored in the header of the light curve files under the keyword CROWDSAP. In cases where a custom/adjusted mask was selected for extracting the signal from the TPFs (Sec. 2.2.2), we (re-)assessed the metric as

$$\text{CROWDSAP}^+ = \frac{f_*}{\sum_k f_k} \quad (2)$$

where  $f_*$  and  $f_k$  are the fluxes from the target and the  $k$ -th source contained in the aperture (including the target), respectively, these being calculated from the TESS magnitudes (Paegert et al. 2021). A comparison between CROWDSAP and the adjusted values yielded minor differences of  $\lesssim 0.01$ , being only higher for the below listed stars HD 111973 and HD 152234.

We provide the contamination metric of the stars in Table A.1. Values close to 1 indicate that the flux from all secondary sources in the aperture contributes minimally to the target light curve, whereas, the photometry becomes less reliable for values of the metric  $\lesssim 0.8$  (Guerrero et al. 2021). The latter case concerns here stars HD 152234 and HD 111973. These are followed by HD 141318 and HD 79186, with CROWDSAP<sup>+</sup> values 0.84 and 0.89, respectively. The rest of the sample displays CROWDSAP<sup>+</sup>  $> 0.9$ , with the vast majority of these stars exceeding 0.95.

Finally, during the inspection of the TPFs (Sect. 2.2.2) we flagged three stars, which could be affected by flux from a bright source that is located outside the photometric aperture. These objects are the above mentioned HD 111973 and HD 79186, as well as HD 94493.

### 2.3. Overlapping TESS studies and reported variables

We checked in TESS studies for overlapping cases and report HD 51309 to have been studied by Burssens et al. (2020) and Bowman et al. (2020) with data from Sectors 1 – 13. We extend

<sup>1</sup> <https://mast.stsci.edu/portal/Mashup/Clients/Mast/Portal.html>

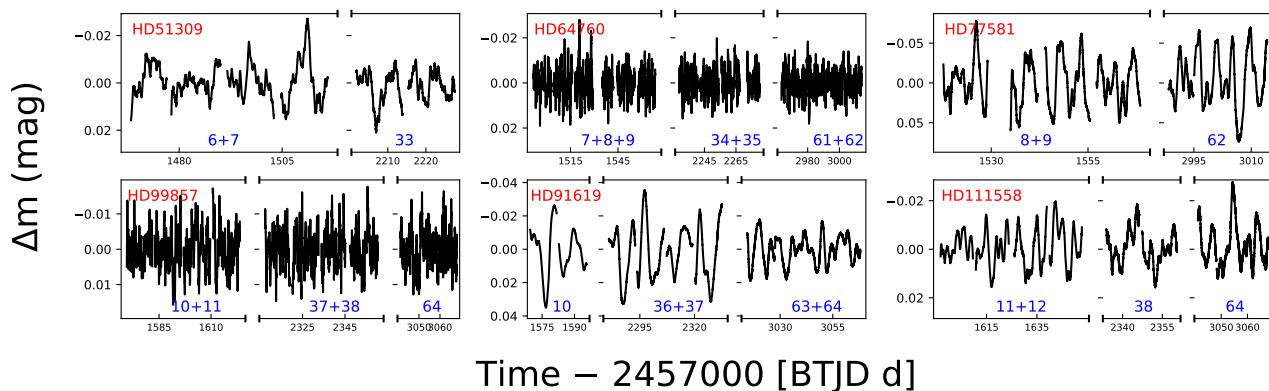


**Fig. 1.** Time-series photometry from TESS of selected BSGs. Data are detrended, normalized, and converted into units of magnitude. For each star, we show data from different sectors over multiple panels. Consecutive sectors are joined together and their numbers are displayed at the bottom of each panel. The light curves of the entire sample are displayed in the Appendix B.

here the variability study to Sector 33 and complement with the time-domain features of the star, measuring also its luminosity from the modeling of multiband photometry.

During a combined cross matching of our stars with the General Catalog of Variable Stars (GCVS; Samus et al. 2017) and the variability study with Hipparcos by Lefèvre et al. (2009), nine stars of the sample were identified as  $\alpha$  Cygni variables<sup>2</sup>. Moreover, three BSGs are reported in Simbad as double/multiple systems: the above discussed for their crowding effect HD 152234 and HD 111973, as well as HD 77581. The latter is the well studied high-mass X-ray system Vela X-1.

### 3. Methodology

The TESS data of the Galactic BSGs display variability of up to  $\sim 0.1$  mag in amplitude, which is described as (quasi-)periodic with dominant frequencies that, for several stars, vary across the different observing windows. We identify cases where variability displays irregular patterns that can be also explained as a superposition of cycles with different periods. At a first glance, the signal of several stars with low photometric amplitude resembles that of instrumental noise (the least luminous BSGs; see Sect. 5), and which typically characterizes the sky objects as “invariant”.

#### 3.1. Extraction of frequencies

To explore the presence of periodic signals in the TESS data, we made use of the `lightcurve.Periodogram` class and computed the Lomb-Scargle periodograms (amplitude spectra). We extracted the prominent frequencies via an iterative pre-whitening process; at each iteration, we selected the frequency with the highest amplitude, fit the light curve with the corresponding sinusoidal model and subtracted it. The residuals of the fit were then subjected to a new iteration for identifying the next peak frequency, and the process was repeated until a termination criterion was met (see Sect. 3.2). The procedure is demonstrated in Fig. 2 for star HD 94493 using the stitched light curves from Sectors 63 and 64.

The frequencies that were extracted from an observing window were categorized into four types using the Rayleigh resolution  $1/\Delta T$ , where  $\Delta T$  is the length of the studied timespan. These types are:

<sup>2</sup> We here account for those stars with a solid classification, disregarding those flagged as candidates.

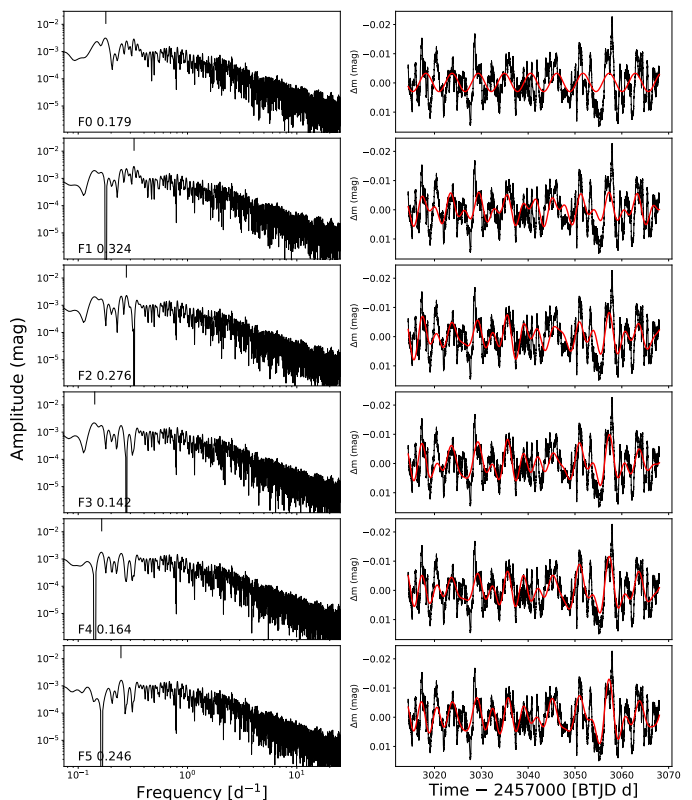


**Fig. 2.** Iterative pre-whitening for the extraction of frequencies for HD 94493 (Sec. 63+64). *Left.* The calculated amplitude spectra (Lomb-Scargle periodograms) shown in logarithmic scale. A vertical line at the top of each panel points to the extracted frequency, which is reported in the lower left. *Right.* The light curve of the star (black points) with superimposed the integrated fit model of sinusoids (red).

- independent frequencies,  $f_i$ . These are significant peaks that are typically identified early in the extraction process and are physically interpreted in BSGs either as opacity-driven  $g$ - $p$ -modes or as the rotational modulation by an aspherical wind and/or surface spots.
- harmonic frequencies, which were identified as integer multiples of the independent ones.
- combinations (algebraic sums) of two previously extracted frequencies.

- frequencies that were repeated within the adopted resolution. These are likely to be spurious detections that emerge during the subtraction of the periodic model, and essentially trace the removed signal. The probability of them being unresolved mode orders of period-spacing patterns (and thus having a physical origin) is too considered.

In addition, we considered credible frequencies those being higher than  $0.07 \text{ d}^{-1}$  in order to resolve a minimum of two cycles per sector. Joining consecutive sectors to form a larger observing window did not lift this constraint, given that the data of the separate sectors were individually normalized, potentially washing out periods longer than  $\sim 14$  days. The total of the independent frequencies and their parameters, subject of our investigation in Sect. 5, are tabulated in Appendix C.

We explored whether the identified frequencies are associated to effects introduced by the stellar rotation, in a similar manner as in Burssens et al. (2020). We calculated the lowest frequency expected from the reported  $v \sin i$  values by Fraser et al. (2010) and our inferred radii (see Sect. 4),

$$\nu_{\text{low}} = \frac{v \sin i}{2\pi R} \sim 0.02 \frac{v \sin i [\text{km s}^{-1}]}{2\pi(R [R_{\odot}])} \text{ d}^{-1} \quad (3)$$

A (conservative) shortest rotational period was also defined using the critical limit for the rotational velocity of a sample star, which is estimated by interpolation of the stellar parameters with the evolutionary models from Ekström et al. (2012). Hereafter, we assign the term cROT (candidate rotating variables) to those stars with (independent) frequencies that can be justified as rotationally induced. Respectively, the term nROT points to the rest, nonrotating variables.

In Fig. 3, we display in logarithmic scale the amplitude spectra of selected BSGs at the beginning (cyan) and the end (red) of the iterative process. Among the datasets from different windows per star, we show the one with the best-fit SLF variability model (see below). We mark the different types of frequencies and highlight the range of values (grey-shaded strip) that can be justified as rotationally induced.

### 3.2. Stochastic low-frequency variability

Altogether the amplitude spectra of the Galactic BSGs illustrate a background signal that is indicative of SLF variability. It has the form of a broad excess in the amplitude at low frequencies (red noise), being then followed by a decline of 1–2 orders of magnitude and reaching the level that is described as white noise. The stochastically-excited signal is parameterized by a Lorentzian-like profile (Stanishev et al. 2002; Blomme et al. 2011) that is typically employed for describing its properties (e.g. Bowman et al. 2019a, 2020; Dorn-Wallenstein et al. 2020; Shen et al. 2024).

At each step of the iterative pre-whitening process, we fit the amplitude (residual) spectra with the function

$$\alpha(\nu) = \alpha_w + \frac{\alpha_0}{1 + (2\pi\nu\tau)^\gamma}, \quad (4)$$

where  $\alpha_0$  the amplitude of the red noise as  $\nu \rightarrow 0$ ,  $\tau$  the characteristic timescale,  $\gamma$  the slope of the decay, and  $\alpha_w$  the white-noise term. The fit of the data was performed in the frequency range  $0.07\text{--}25 \text{ d}^{-1}$  using the `optimize.curve_fit` routine from the `scipy` package (Virtanen et al. 2020). The error estimates were assessed from the covariance matrix. We evaluated the quality of the fit using a standard  $\chi^2$  calculation.

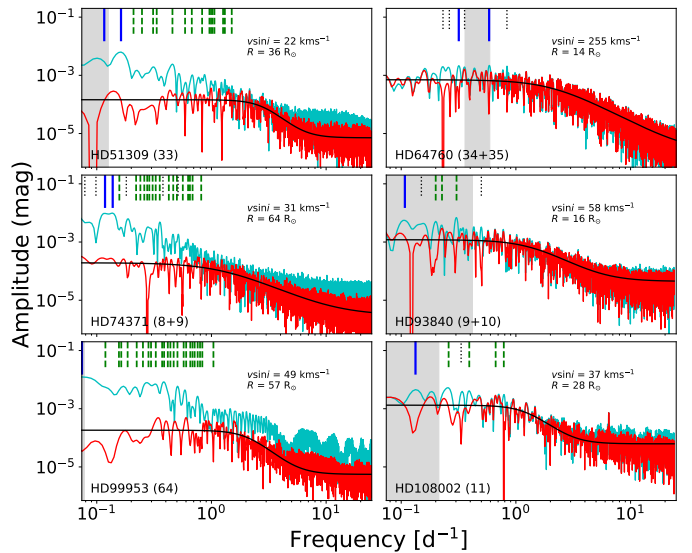


**Fig. 3.** Frequency spectra of selected BSGs. We show the periodograms calculated at the beginning (cyan) and the end (red) of the pre-whitening process. The vertical lines at the top of each panel point to different types of the identified frequencies; independent (solid), harmonics (dashed), and combinations (dotted). The solid black line corresponds to the best-fit SLF variability model (Eq. 4) that we adopt for the star. The grey-shaded region indicates the range of frequencies that can be identified as due to the stellar rotation. We display the data for the entire sample in the Appendix B.

We terminated the iterative process as soon as the relative change between the  $\chi^2$  values of two successive iterations fell below the tolerance value of 0.1 for five iterations in a row. The signal-to-noise (S/N) values of the prior extracted frequencies were then updated in order to comply with the latest computed model. For describing the SLF variability of a star with multiple observing windows, we adopted the fit model with the lowest  $\chi^2$ , which we display in logarithmic scale in Fig. 3 (black curve). The 10-base logarithm of the fit values of  $\alpha_0$  and  $\alpha_w$ , along with the values of  $\tau$  and  $\gamma$ , are listed in Table A.2.

### 3.3. Metrics of the time domain

As for a statistical measure of the photometric scatter, we calculated the standard deviation of the magnitude measurements  $X_i$

$$\sigma = \sqrt{\frac{\sum_{i=1}^N (X_i - \bar{X})^2}{N}} \quad (5)$$

where  $\bar{X}$  is the mean magnitude of the light curve and  $N$  the number of datapoints. The alternative and less sensitive to outliers median absolute deviation was also explored; as it delivered almost identical to  $\sigma$  results, it is here omitted.

A robust method to assess the independence of successive measurements is the coherency parameter,  $\psi^2$ . It characterizes the level of stochasticity in the time series data by evaluating the correlation between the sequential measurements against the white noise. It is defined on the basis of the zero-crossings  $D_k$ , namely the number of times that the signal crosses the zero level. The non-negative integer  $k$  is the order in the time-series differences, such that

$$X_{k,i} = X_{k-1,i} - X_{k-1,i-1} \quad (6)$$

with  $X_{0,i}$  pointing to the original dataset  $X_i$ . For measuring  $D_k$ , the “clipped” data points  $Z_{k,i}$  are first generated from  $X_{k,i}$  as

$$Z_{k,i} = \begin{cases} 1, & \text{if } X_{k,i} \geq 0 \\ 0, & \text{if } X_{k,i} < 0 \end{cases} \quad (7)$$

wherefrom  $D_k$  is calculated as the sum of the squared consecutive differences and normalized to their size,

$$D_k = \frac{1}{N - k - 1} \sum_{i=2}^N (Z_{k,i} - Z_{k,i-1})^2, \quad (8)$$

Finally,  $\psi^2$  is calculated sufficiently from the first 5 orders (Kuzlewicz et al. 2020) as

$$\psi^2 = \sum_{k=0}^4 \frac{(\Delta_k - \phi_k)^2}{\phi_k} \quad (9)$$

where  $\Delta_k$  denotes the increments of the  $k$ -order crossings, i.e.

$$\Delta_k = \begin{cases} D_0, & \text{for } k = 0 \\ D_k - D_{k-1}, & \text{otherwise,} \end{cases} \quad (10)$$

and  $\phi_k$  being the respective increments of a white-noise signal. The latter values were calculated from a Gaussian-distributed sample of datapoints that was generated over the studied grid of the TESS timestamps.

Finally, we evaluated the asymmetry of the light curves using the moment measure of skewness, which is defined as

$$\text{skw} = \frac{\sum_{i=1}^N (X_i - \bar{X})^3}{N\sigma^3} \quad (11)$$

The metric has a positive (negative) value when the distribution of measurements is right (left) skewed, and equals to zero when it is symmetric.

The calculated values of the above statistical measures are provided in Table A.2. These were taken as the average values of measurements obtained across the different observing windows. Uncertainties are taken as the 1-sigma values.

#### 4. Spectral energy distributions

Our aim is to investigate the association between variability features and fundamental stellar parameters. While  $\log T_{\text{eff}}$  and  $\log g$  for our sample stars have been determined by Fraser et al. (2010), their analysis did not provide stellar luminosities. To retrieve these, we modeled the spectral energy distribution (SED) of the objects.

We constrained the blue part of the SEDs with UVB photometry from Mermilliod (2006) and with data from the Naval Observatory Merged Astrometric Dataset (NOMAD; Zacharias et al. 2004) that extend to the  $R$  band. We included recent photometry from *Gaia* DR3 in  $G$ ,  $G_{\text{BP}}$  and  $G_{\text{RP}}$  bands, that in general was found to be in good agreement with the earlier measurements. Near-infrared photometry was taken from 2MASS (Cutri et al. 2003), whereas data from the AllWISE catalog (Cutri et al. 2014) were employed for describing the SEDs up to  $22 \mu\text{m}$ . To better constrain the flux in the mid-infrared, we also included photometry from the AKARI satellite (Ishihara et al. 2010) and the Midcourse Space Experiment (MSX; Egan et al. 2003). We collected the photometric counterparts by cross-matching between the stellar coordinates and the above catalogs, using a

search radius of  $2''$  for the optical and 2MASS studies and  $5''$  for the mid-infrared ones that have a lower spatial resolution. The conversion between magnitudes and fluxes was performed based on the passband zeropoints and effective wavelengths, which are available by the SVO Filter Profile Service<sup>3</sup>.

We fitted the multiband photometry within a standard optimization procedure using the public available grids of synthetic spectra generated with the TLUSTY code (OSTAR2002 & BSTAR2006; Lanz & Hubeny 2007). We selected model SEDs with solar abundances. As the lower limit of the BSTAR2006 grid is 15 000 K, we fit the data of our cooler seven stars with theoretical SEDs from Howarth (2011), which are generated with the ATLAS9 code.

The flux  $f_\lambda$  at wavelength  $\lambda$  that is received from a star with radius  $R$  at distance  $D$  and reddened with extinction  $A(\lambda)$ , is given as

$$f_\lambda = C^2 F_\lambda 10^{-0.4A(\lambda)} \quad (12)$$

where  $F_\lambda$  is the flux emerging from the stellar surface and  $C = R/D$ . We ran a Levenberg-Marquardt method to minimize the residuals between Eq. (12) and the photometry, setting free the scaling factor  $C$  and the visual extinction  $A_V$  (e.g. as in Kourniotis et al. 2015, 2022). Relative to the latter, the extinction at  $\lambda$  was expressed using the law of Cardelli et al. (1989) assuming  $R_V = 3.1$ . The flux per unit surface area,  $F_\lambda \equiv F_\lambda(T_{\text{eff}}, \log g)$ , was determined for each star by interpolating within the grid of synthetic models.

The photometry and best-fit models for selected stars are displayed in Fig. 4, and for the entire sample in Appendix B. For several cases, a weak offset between the model flux and the observations in the infrared implies excess due to stellar winds. In Table A.3, we list the 10-base logarithms of  $C$  (expressed in units of  $R_\odot/\text{pc}$ ) that are used for determining the stellar radii, thus luminosities, from the distances to the objects. In this work, the latter values were taken as the photogeometric estimates from *Gaia* DR3 (Bailer-Jones et al. 2021) and are listed in Table A.3, along with the resulting  $\log(L/L_\odot)$  values.

#### 5. Results and discussion

In the current section, we present and discuss associations between the physical and evolutionary properties of the stars and the features extracted from the analysis of variability.

With the stellar luminosities measured, we locate our studied objects in the Hertzsprung–Russell diagram of Fig. 5, and superimpose them on models of stellar evolution at solar metallicity (Ekström et al. 2012). The tracks assume an initial rotational velocity at 40% of the critical speed. As can be seen, the sample stars span evolutionary tracks beyond the end of the main-sequence phase in the range  $M_{\text{ini}} = 9 - 40 M_\odot$ . In the same plot, we indicate the reported  $\alpha$  Cygni variables using large outer circles, which occupy the upper right region of the evolutionary diagram. Being in a good agreement with their definition as post-RSGs, they span tracks that suggest evolution bluewards ( $5.0 \lesssim \log(L/L_\odot) \lesssim 5.8$ ).

As for an inherently spectroscopic assessment and alternative to the SED-based luminosity, we additionally calculated the Eddington factor  $\Gamma_e$  of the studied objects (Table A.3). Being function of the so-called spectroscopic luminosity (Langer & Kudritzki 2014),  $\Gamma_e$  is defined as

$$\Gamma_e \equiv \frac{\kappa_e L}{4\pi G M c} = \frac{\sigma_B \kappa_e T_{\text{eff}}^4}{c g} \quad (13)$$

<sup>3</sup> <http://svo2.cab.inta-csic.es/theory/fps/>

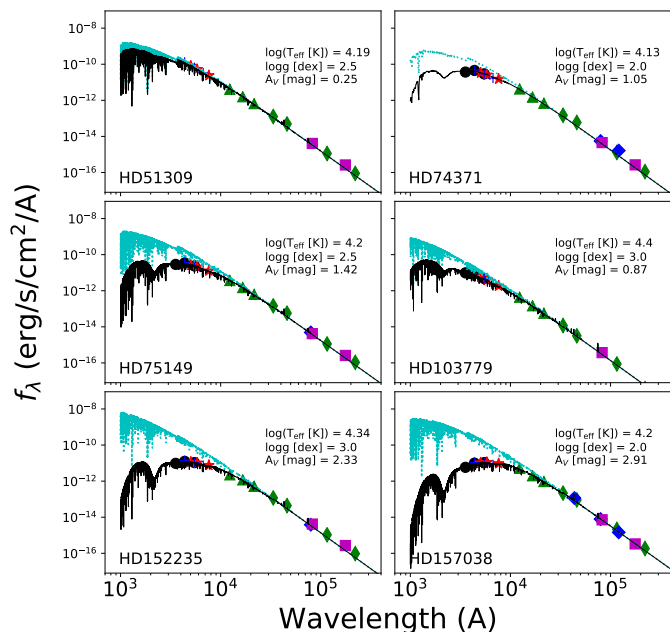


**Fig. 4.** Spectral energy distributions of selected BSGs. Data were taken from Mermilliod (2006) (black circles), NOMAD (blue crosses), *Gaia* DR3 (red asterisks), 2MASS (green triangles), WISE (green rhombi), AKARI (magenta squares), and MSX (blue diamonds). The best-fit TLUSTY model (ATLAS9 for HD 74371) is overplotted, unreddened (cyan line) and reddened according to the inferred  $A_V$  (black line). In each panel, we display the stellar designation (lower left) and parameters (upper right). The modeled SEDs of the entire sample are displayed in the Appendix B.

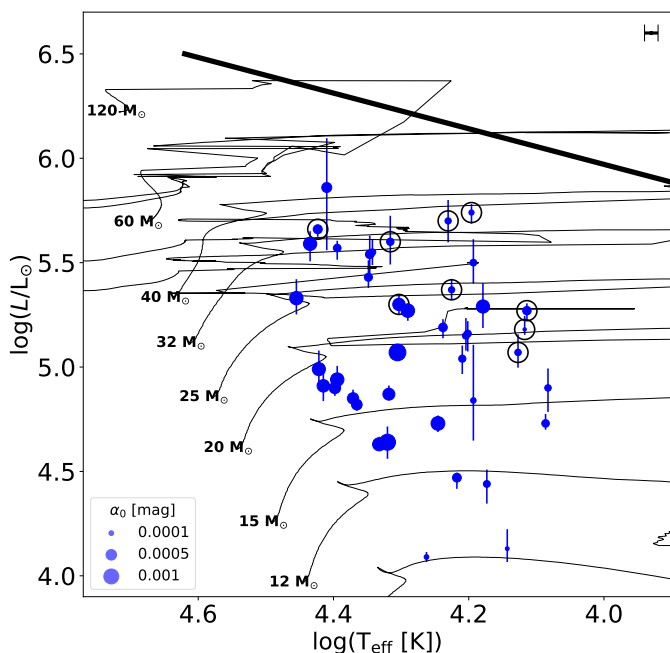


**Fig. 5.** Hertzsprung–Russell diagram for the evolution of massive stars. Theoretical tracks at solar metallicity are taken from Ekström et al. (2012), for stars rotating initially at 40% of their critical velocity. The size of the markers is proportional to the amplitude of the SLF variability (Sect. 5.3). The variables of the  $\alpha$  Cygni class are indicated by outer circles, and the thick line represents the Humphreys–Davidson limit. The uncertainty in the spectroscopic temperature is illustrated by the errorbar on the upper right.

where  $\sigma_B$  is the Stefan–Boltzmann constant,  $c$  the speed of light, and  $\kappa_e = 0.4 \text{ cm}^2 \text{ g}^{-1}$  the opacity, here assuming only due to photon scattering by free electrons.

### 5.1. Correlations in the time domain

In Fig. 6, we present the plots of  $\log T_{\text{eff}}$ ,  $\log(L/L_{\odot})$ , and  $\Gamma_e$  against the calculated metrics of the time domain. We distinguish between the cROT (red markers) and nROT (black markers) variables, and indicate the reported variables of the  $\alpha$  Cygni class as in Fig. 5. Moreover, we indicate stars susceptible to contamination in their light curves, showing CROWDSAP+ values lower than 0.8 (“X” symbols) and within 0.8 – 0.9 (“x” symbols). To the latter set of stars, we added HD 94493 for a possible such effect caused by a bright star external to the TESS aperture (Sect. 2.2.3). To assess whether the relationship between two parameters is monotonic, we show at the lower right of each panel the Spearman’s rank correlation coefficient  $r_s$ . Outliers were excluded from this calculation by masking values whose absolute difference from the median exceeded five times the median absolute deviation.

The strongest correlation found in this study is the positive trend between  $\sigma$  and  $\log(L/L_{\odot})$  ( $r_s = 0.74$ ,  $p < 0.0001$ ), which decodes into a more tight relationship with  $\Gamma_e$  ( $r_s = 0.77$ ,  $p < 0.0001$ ). Such a correlation is already reported by the early variability studies of BSGs (Maeder & Rufener 1972; Maeder 1980), and mirrors, to a certain extent<sup>4</sup>, the corresponding trend that is reported between the luminosity and the amplitude of SLF variability (Bowman et al. 2019a, 2020). Here, the extreme outlier star ( $\sigma \sim 0.03$ ) is the  $\alpha$  Cygni variable HD 77581 (Fig. 1), which as previously mentioned is a member of the eclipsing binary Vela X-1; the star is long known to possess an enigmatic light curve that is modulated by effects such as, gravitational distortion (Jones & Liller 1973), gas streaming (Blondin et al. 1991), and non-radial oscillations of the BSG being tidally induced by the companion pulsar (Quaintrell et al. 2003).

Positive correlation is also seen between  $\psi^2$  and  $\log(L/L_{\odot})$  ( $r_s = 0.52$ ,  $p < 0.001$ ), indicating that the more luminous (and higher amplitude) variables possess smooth light curves with a higher degree of coherency compared to less luminous ones (e.g., also Bowman & Dorn-Wallenstein 2022). Moreover, the highest  $\psi^2$  values are found to largely fluctuate across different TESS sectors. With several of these cases being flagged as cROT variables, these stars could expose an ephemeral modulation induced by rotation that emerges on top of their pulsational activity. On the other hand, the less luminous BSGs ( $\log(L/L_{\odot}) < 5$ ) are prone to a noise-like photometric behavior, being further identified in their vast majority as cROT stars. Their variability may therefore be explained by the presence of surface spots and/or co-rotating inhomogeneities in the wind (Morel et al. 2004; Aerts et al. 2013; Balona et al. 2015; Burssens et al. 2020), with the latter features growing with increasing mass loss (thus with increasing luminosity; Krtićka et al. 2021). The positive correlation between  $\Gamma_e$  and the skewness ( $r_s = 0.33$ ,  $p = 0.04$ ; Fig. 6) could credit the latter scenario; winds structured by line-driven instabilities are linked to short-term brightening of the stars, producing thus time series that are negatively skewed (Krtićka & Feldmeier 2021).

Several  $\alpha$  Cygni variables within the upper luminous sample appear to be less bound to the above trends. Moreover, other lu-

<sup>4</sup> Particularly for stars that do not display significant isolated frequencies.

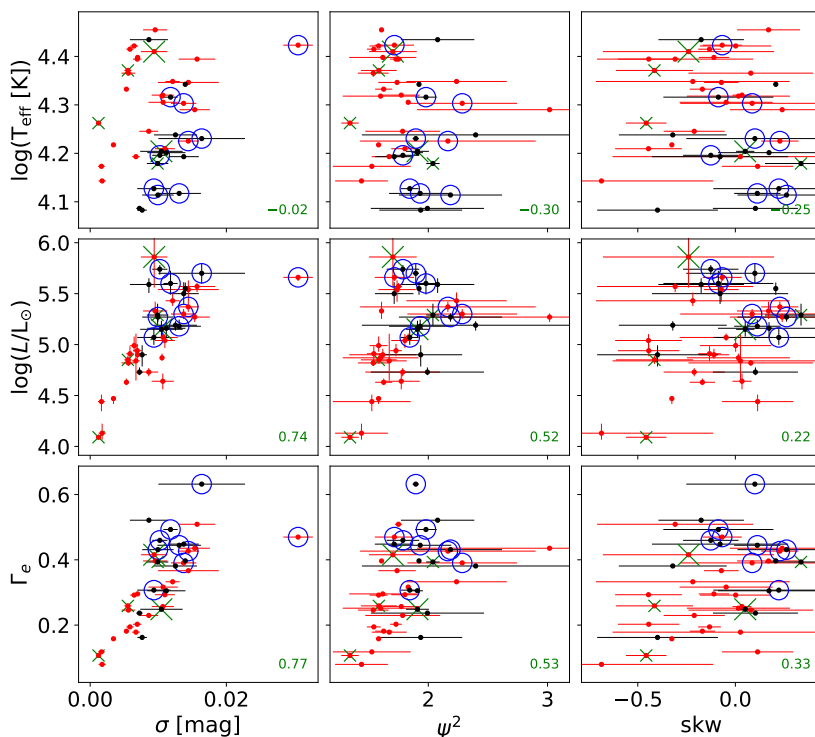


**Fig. 6.** Plots of the stellar parameters of BSGs against their time-domain statistics. Red points indicate the cROT variables, and black points the nROT ones. The outer circles indicate the  $\alpha$  Cygni variables. We mark stars susceptible to TESS contamination with CROWDSAP+ values lower than 0.8 (“X” symbols) and within 0.8 – 0.9 (“x” symbols). To the latter stars, we added HD 94493 due to its proximity to a bright source located outside the photometric aperture.

minous stars<sup>5</sup> ( $\log(L/L_{\odot}) \gtrsim 5.1$ ), as well as the less luminous nROT variable HD 105071 (with  $\psi^2 = 2.0 \pm 0.5$ ; Fig. 6), exhibit the  $\alpha$  Cygni phenomenon in their light curves, and are marked as “candidate”  $\alpha$  Cygni variables in the Hipparcos study of Lefèvre et al. (2009). Collectively, the irregularity in the photometric data of these objects follows the realization that they are not homogeneous with respect to the excitation mechanisms of their pulsations, these including oscillatory convection modes and radial strange modes (Gautschi 2009; Saio 2011; Saio et al. 2013). On top of this activity, a structured and/or variable wind has been reported in stars of the class (Chesneau et al. 2014; Kraus et al. 2015; Cidale et al. 2023).

## 5.2. Correlations with the independent frequencies

In Fig. 7, we display the total of the independent frequencies  $f_i$  extracted and their amplitudes  $A_i$  as function of the  $\log T_{\text{eff}}$  (upper panel) and  $\log(L/L_{\odot})$  (lower panel). The data are color coded as function of the S/N. The number of the frequencies  $f_i$  per observing window does not exceed three. Accordingly, the number of “individual” frequencies per star (under the Rayleigh resolution) that were extracted from the different windows is less than five. Nonetheless, no clear association is found between these metrics and the stellar parameters. We note a disposition of the hotter and less luminous BSGs toward higher frequencies. With the latter showing the lowest S/N values, such an observation is apparently sensitive to the extraction process followed (e.g. the termination criterion for the prewhitening process and the noise or significance level adopted). The distribution of  $A_i$  mirrors that

of  $\sigma$  (Fig. 6), linking the photometric dispersion of stars with  $\log(L/L_{\odot}) \gtrsim 5$  to significant (quasi-)periodic cycles, whereas moving to the less luminous BSGs, variability is rather described as blends of weak low-amplitude signals.

A more comprehensive view of the latter plot is gained in the histograms of Fig. 8, which show the distribution of  $f_i$  as function of  $\log T_{\text{eff}}$  (upper panel) and  $\log(L/L_{\odot})$  (lower panel). For building the histograms, we employed the individual frequencies per star, i.e. we grouped the frequencies extracted from the different windows together and bin averaged. The size of the bin was chosen to be  $0.05 \text{ d}^{-1}$  and approximate to the Rayleigh resolution. Then, for each of the two stellar parameters we split the sample by the 33rd and 66th percentile, forming three nearly equal size groups. Their histograms are illustrated with different color/shape; solid blue ( $p_0$  to  $p_{33}$ ), dashed green ( $p_{33}$  to  $p_{66}$ ), and dotted red ( $p_{66}$  to  $p_{100}$ ). The interval parameter values are given in the legend. As the data display positive skewness, we fit the histograms to gamma distributions following the two-variable parameterization, with a probability density function of

$$f(x, \alpha, \beta) = \frac{\beta^{\alpha} x^{\alpha-1} e^{-\beta x}}{\Gamma(\alpha)} \quad (14)$$

where  $\Gamma(\alpha)$  is the gamma function. The calculated fit models are displayed in Fig. 8 as thick curves; their parameters are provided in the legend.

The inspection of the grouped data as function of the stellar temperature (Fig. 8, upper panel) reveals that the hot BSGs of the sample with  $\log T_{\text{eff}} \geq 4.34$  display shift of their frequencies to higher values. The high-frequency tail recedes with decreasing temperature such that, in the cooler groups, frequencies become heavily centered around  $\sim 0.13 \text{ d}^{-1}$ . This effect, however, is produced by the higher fraction of the contained  $\alpha$  Cygni variables;

<sup>5</sup> HD 92964, HD 108002, HD 109867 ( $\psi^2 = 2.2 \pm 0.4$ ), HD 111973, HD 115842, HD 152235, and HD 154090.



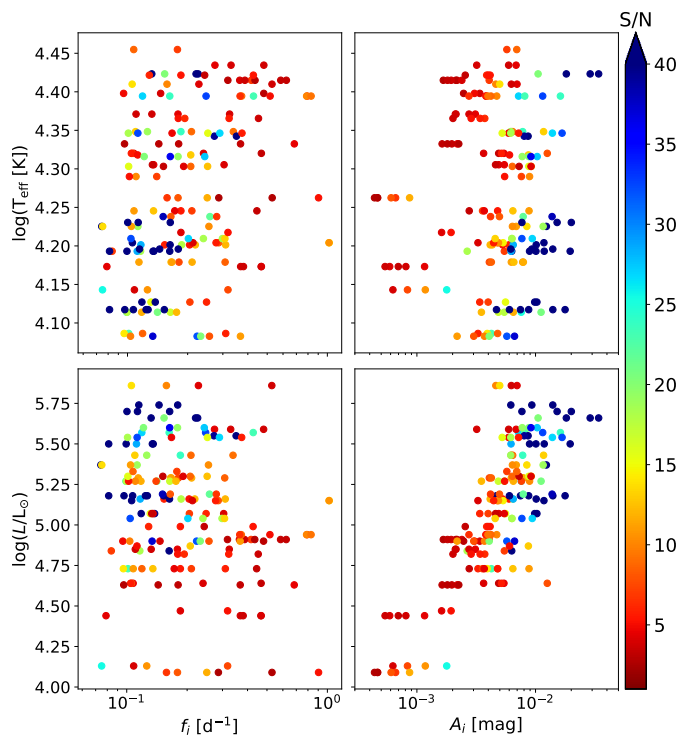


**Fig. 7.** Plots of stellar parameters against the frequencies  $f_i$  and their amplitudes  $A_i$ , which are extracted from the periodograms of all observing windows. The data are color coded with respect to their S/N.

the distribution of the latter is shown on the plots as hatched histograms. Their identified frequencies are dispersed modestly around the latter value and confined below  $0.3 \text{ d}^{-1}$ . Moving into the statistics on the stellar luminosity (Fig. 8, lower panel), one can tell that the aforementioned tail identifies stars of the low- and moderate-luminous groups, which share similar properties.

Summing up, the periodograms differentiate between distinct groups of stars that fall under the BSG umbrella: moderate/high-luminous stars showing frequencies at the lower range, the subgroup of  $\alpha$  Cygni stars with  $f_i < 0.3 \text{ d}^{-1}$ , and the younger and less massive BSGs with frequencies shifted to higher values. As the latter group refers to more compact objects per se, we speculate that this effect is caused by the rotational modulation acting over shorter periods and/or to the effects that the Coriolis force exerts on the excited modes, although the latter mechanism has been mostly observed in B-type stars in the main sequence (e.g. Salmon et al. 2014).

### 5.3. Correlations with the stochastic low-frequency variability

In a similar way to Fig. 6, we show plots of the stellar parameters against the parameters of the SLF variability in Fig. 9. To discuss the dependence of the latter on the evolutionary stage of the stars, we re-calculated the Spearman’s rank correlation coefficient for each parameter set having excluded the  $\alpha$  Cygni stars (bold font value).

A significant positive correlation is seen between the red-noise amplitude and  $\log T_{\text{eff}}$  ( $r_s = 0.59, p < 0.0001$ ) that persists with excluded (and within) the group of  $\alpha$  Cygni variables ( $r_s = 0.53, p = 0.002$ ). This information is illustrated on the Hertzsprung–Russell diagram (Fig. 5) by setting the marker size to being proportional to  $\alpha_0$ . Our results suggest that the background signal is more pronounced at earlier stages of evolution

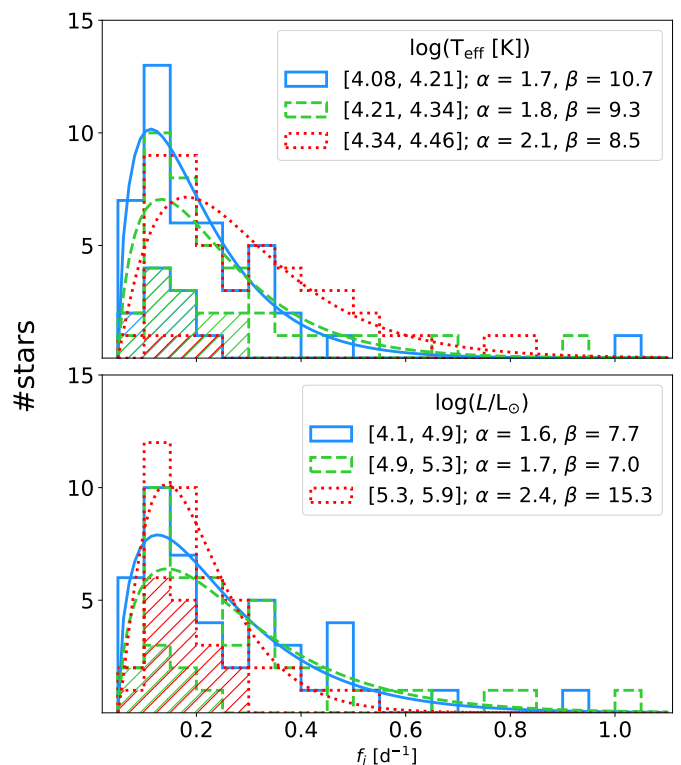


**Fig. 8.** Histograms of the individual BSG frequencies as function of  $\log T_{\text{eff}}$  (upper panel) and  $\log(L/L_{\odot})$  (lower panel). In each plot, the sample is split into three groups based on their parameter values (legend). The histograms for the  $\alpha$  Cygni variables are indicated with a dashed surface.

and drops as the stars age. Interestingly, an inverse association between these two parameters has been reported by studies on early-type stars spanning the upper main sequence (Bowman et al. 2020; Shen et al. 2024). Complementing with the present findings over a more evolved sample lets us speculate that SLF variability is amplified at or shortly after the end of the main-sequence phase.

From Fig. 9, it can also be seen that the characteristic timescale  $\tau$  is negatively correlated with  $\log T_{\text{eff}}$  ( $r_s = -0.28, p = 0.08$ ), which is in line with the reported decrease in the corresponding characteristic frequency of the signal toward more evolved stars (Shiode et al. 2013; Bowman et al. 2020; Vanon et al. 2023; Shen et al. 2024). The nonsignificant positive trend between  $\tau$  and  $\Gamma_e$  ( $r_s = 0.23$ ) then mirrors the inverse association of the former with  $\log g$ , whereas no association is seen between  $\tau$  and  $\log(L/L_{\odot})$ . The slope  $\gamma$  of the red noise, on the other hand, is shown to be most related with  $\log(L/L_{\odot})$ , though nonsignificantly ( $r_s = 0.18$ , when excluding the  $\alpha$  Cygni stars<sup>6</sup>). Weak (or no) correlations are observed between the stellar parameters and the level  $\alpha_w$  of the white noise.

Studies of young massive stars have highlighted the positive trend between the amplitude of SLF variability and luminosity (e.g. Bowman et al. 2020; Shen et al. 2024), which are interpreted as due to the larger convective velocities with increasing stellar mass and luminosity of the core (e.g. Shiode et al. 2013; Ratnasingam et al. 2023; Anders et al. 2023). This trend is discussed to be insensitive to the parameter of metallicity, which

<sup>6</sup> The outlier nROT star with  $\gamma \sim 6$  is HD 105071, which as earlier mentioned is a candidate  $\alpha$  Cygni variable. Given also its large  $\psi^2$  value, we suggest that the distance to the target may be underestimated.

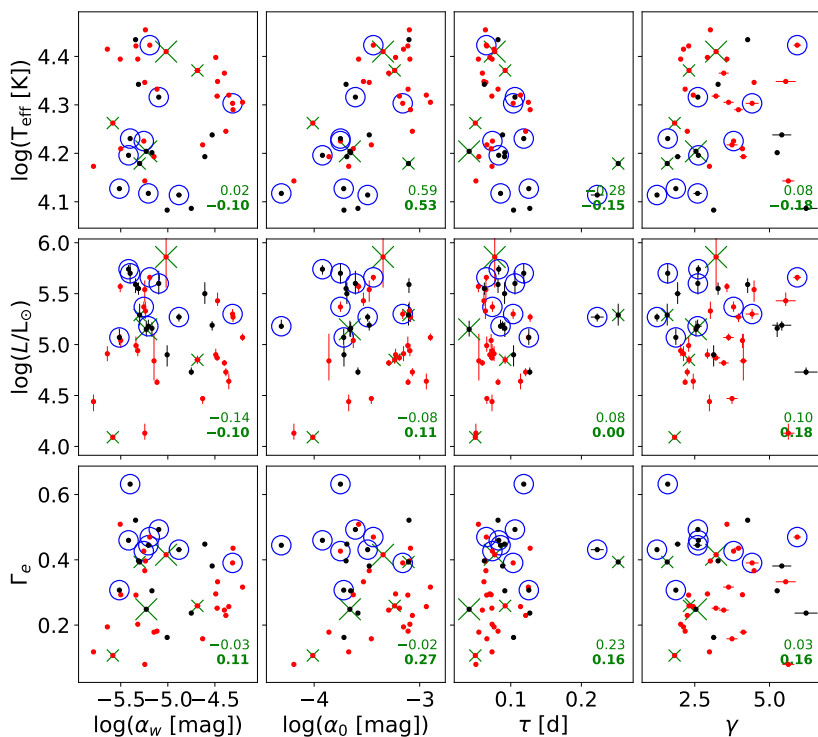


**Fig. 9.** Same as in Fig. 6, for the parameters  $\log \alpha_w$ ,  $\log \alpha_0$ ,  $\tau$ ,  $\gamma$ , of the SLF variability models. The bold font value shows Spearman's rank correlation coefficient for a set of parameters, having excluded the  $\alpha$  Cygni variables.

serves as an evidence of the core-excited nature of the background signal, especially for stars at young stages (Bowman et al. 2019b, 2024). At first glance, the analysis of the current, post-main-sequence, sample suggests that  $\log \alpha_0$  and the stellar (and spectroscopic) luminosities are unrelated (Fig. 9). A positive, yet nonsignificant, trend between these parameters is shown when one excludes the  $\alpha$  Cygni variables.

We compare the questionable latter trend to the relevant findings from Bowman et al. (2019b) in the LMC. Using TESS data, these authors extracted the parameters of the SLF variability from 53 BSGs with spectral type earlier than B4. For our purpose we calculated, and provide in Table A.3, the absolute magnitudes in  $G$ -band of our sample stars from

$$M_G = G - 5 \log_{10} D + 5 - A_G \quad (15)$$

using the values of distance  $D$  from *Gaia* (Table A.3). The  $G$ -band extinction was estimated from our SED-estimated extinction in the visual considering that  $A_G \approx 0.77A_V$  (Sanders & Das 2018).

In Fig. 10, we display  $M_G$  against  $\log \alpha_0$ , color coding the markers as function of  $\log T_{\text{eff}}$ . The variables of the  $\alpha$  Cygni class (with large outer circles) appear confined below  $-6.4$  mag (vertical thin line). Considering that possible unidentified  $\alpha$  Cygni stars would occupy the same area on the plot (see also Sect. 5.1), we focus on the 25 BSGs that are fainter than this threshold. As expected from our above discussion, a nonsignificant weak (negative) trend is measured between the amplitude of the SLF variability with decreasing  $M_G$  ( $r_s = -0.08$ ). We depict the linear fit to the truncated sample using a solid thick line.

An important remark in the study by Bowman et al. (2019b) is the absence of coherent frequencies in the LMC sample, which led the authors to proceed in modeling the SLF variability without pre-whitening their data. As the latter process wears down the amplitude spectra (e.g., see Fig. 3), the relevant properties

are expected to be systematically offset compared to when the original data are modeled instead<sup>7</sup>. Such a speculation is also evident within the study of Bowman et al. (2019b) where a sample of eclipsing stars was explored additional to their BSGs, nevertheless following pre-whitening of their signal peaks. When comparing between those two samples, the measured values for the red-noise level are shown to be systematically offset (their Fig. 4). We display the fit model from the discussed study in our Fig. 10 as a dashed thick line. For the sake of comparison, an arbitrary constant is added to it in order to match the mean level of our data<sup>8</sup>.

Similar trends are found between the study of Bowman et al. (2019b) and the current work when confining ourselves to lower luminosities (Fig. 10). In this regime, one may speculate about a metallicity-independent mechanism for driving the SLF variability, such as core convection. Furthermore, as seen in Fig. 9, the vast majority of variables with  $\log(L/L_\odot) \lesssim 5$  display  $2 \lesssim \gamma \lesssim 4$ , which match, in general, the power-law exponents of the model spectra generated by core-excited IGWs (Edelmann et al. 2019). We do stress that a larger statistical sample is essential for establishing the present result, given the sparsity of our sample toward the low-luminosity end where also the TESS data of HD 141318 are susceptible to contaminating flux ( $\text{CROWDSAP}^+ = 0.842$ ). The results from the current study make also less plausible the scenario that SLF variability is generated by sub-surface convection zones driven by the iron opacity peak. The convective flux in such zones relative to the total stellar flux is expected to increase with decreasing  $\log T_{\text{eff}}$  and increasing luminosity (Cantiello et al. 2021; Shen et al. 2024), which does not comply with the current picture for the SLF variability am-

<sup>7</sup> For testing purposes, we explored our sample using the original amplitude spectra and confirm the effect.

<sup>8</sup> This constant accounts also for the conversion among units.

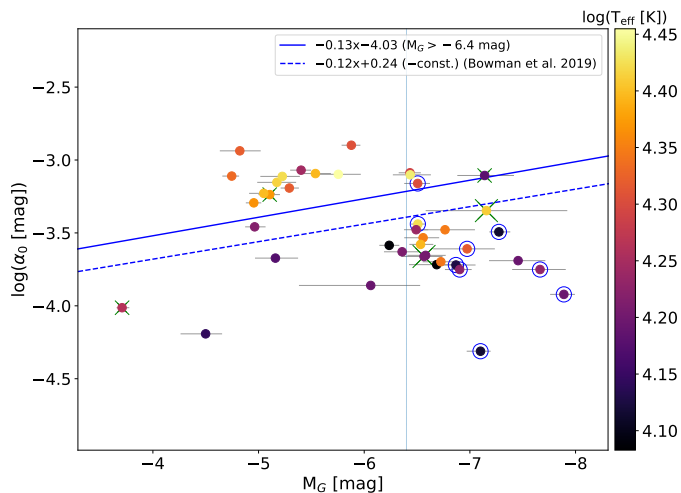


**Fig. 10.** Absolute  $G$ -band magnitudes vs  $\log \alpha_0$ . The markers are color coded as function of  $\log T_{\text{eff}}$ . The designation for the  $\alpha$  Cygni variables and for stars susceptible to TESS contamination follows that in Fig. 6. We show the linear fit to BSGs with  $M_G$  fainter than  $-6.4$  mag (thick solid line). The fit (+offset) to the respective parameters of BSGs in the LMC is displayed (dashed line; Bowman et al. 2019b).

plitude; instead, we observe a decline in  $\alpha_0$  toward the upper cool Hertzsprung–Russell diagram (see Fig. 5).

From Fig. 9, it is also evident that “within” the  $\alpha$  Cygni group no trend is evident between  $\log \alpha_0$  and our both luminosity assessments (accordingly, between  $\log \alpha_0$  and  $M_G$ , for  $M_G \lesssim -6.4$ ; Fig. 10). Rather, these stars are en masse predisposed to lower SLF variability amplitudes. As the stellar age appears in this study to be more influential for the latter parameter compared to the mass, we attribute this effect to the advanced evolutionary stage of  $\alpha$  Cygni stars. In the scenario that the SLF variability is core-excited, the suppressed signal of  $\alpha$  Cygni variables could mirror stars with undersized cores, e.g. due to efficient mixing of the core material into the stellar envelope at the earlier phases. An alternative explanation would point to radiative damping of the low-frequency modes when these propagate within a density stratified envelope, with the effect becoming more prominent with the stellar age (e.g. Vanon et al. 2023). Finally, the positive association that is seen in the early stages between the red-noise amplitude and the stellar mass (Bowman et al. 2020; Shen et al. 2024) is expected to diminish upon a steep drop of the latter, as this can happen during the RSG phase via pulsation-driven superwinds (Yoon & Cantiello 2010).

## 6. Conclusions

In the present work, we undertook a variability study of 41 post-main-sequence BSGs in the Galaxy with parameters ( $\log T_{\text{eff}}$ ,  $\log g$ ) determined from FEROS spectroscopy (Fraser et al. 2010) and our own SED modeling to retrieve stellar luminosities. Alongside, the Eddington factor  $\Gamma_e$  of the stars was explored. Our analysis was performed using data from the TESS survey across Sectors 5–66. We described the photometric time domain by means of three statistical measures; the standard deviation, the coherency parameter  $\psi^2$ , and the skewness, to assess the degree of scatter, stochasticity and asymmetry of the light curves, respectively. In the frequency domain, we extracted prominent frequencies via iterative pre-whitening and modeled the background signal, indicative of SLF variability, that manifests ubiquitously in the residual spectra.

We report a positive correlation between  $\log(L/L_\odot)$  and the amplitude of the TESS light curves. Stars with  $\log(L/L_\odot) \lesssim 5$  display independent frequencies that comply with the rotational ones, suggesting rotational modulation as a plausible mechanism for their variability. The majority of these stars display light curves with negative skewness, which has been shown to be associated with line-driven wind instability. For  $\log(L/L_\odot) \gtrsim 5$ , our sample is further populated by the reported  $\alpha$  Cygni variables (and presumably more unidentified counterparts of the class), which possess multiperiodic variability with diverse, in some cases time-variant, properties. The irregular light curves of these stars mirror the documented and diverse mechanisms acting, such as mixed-mode oscillations including radial strange modes, winds, and (at least for HD 77581) binarity.

A significant positive correlation is found between  $\log T_{\text{eff}}$  and the amplitude of the SLF variability, indicating that the ambiguous signal is more pronounced at earlier phases and drops as the stars evolve beyond the main sequence. Essentially, this result contradicts the scenario that SLF variability is excited by sub-surface convection where the opposite effect would be anticipated. Consistent with previous findings, a negative (positive) association is seen between the characteristic timescale of the signal and  $\log T_{\text{eff}}$  (respectively,  $\Gamma_e$ ).

We report that the amplitude of SLF variability scales weakly with the absolute  $G$ -band magnitude for stars fainter than  $M_G \sim -6.4$  mag, the limit that here confines the  $\alpha$  Cygni variables. Although being nonsignificant, this trend is similar to that for BSGs in the LMC (Bowman et al. 2019b), which may credit the scenario that the background signal is driven by core-excited IGWs. On the other hand, the discussed trend is vanished within the group of  $\alpha$  Cygni variables, with the latter stars being predisposed to lower SLF variability amplitudes. Given that the stellar age appears in this work to be the most potent parameter in regulating the excitation of the signal, we suggest that the suppressed SLF variability of the  $\alpha$  Cygni variables could mirror their rather advanced phase as post-RSG stars.

A study over a larger statistical sample would essentially enable a more improved mapping of variability in BSGs onto the evolutionary diagram. Moreover, theoretical insights to the internal or surface processes of  $\alpha$  Cygni stars are needed for interpreting their distinctive red noise. It is yet to be determined whether these stars undergo changes in the deep interior that can be assistive to their mass loss at the RSG phase, providing at the same time an explanation of their poorly explained surface abundances.

*Acknowledgements.* We thank the anonymous referee for providing a detailed report that greatly improved the quality of this work. The project has received funding from the European Union’s Framework Programme for Research and Innovation Horizon 2020 (2014–2020) under the Marie Skłodowska-Curie grant agreement no. 823734. LC acknowledges financial support from CONICET (PIP 1337) and the University of La Plata (Programa de Incentivos 11/G160). The Astronomical Institute Ondřejov is supported by RVO:67985815. MRD acknowledges support from a CONICET fellowship. This research has made use of the SIMBAD data base, operated at CDS, Strasbourg, France.

## References

- Aerts, C., Bowman, D. M., Símón-Díaz, S., et al. 2018, MNRAS, 476, 1234
- Aerts, C., Lefever, K., Baglin, A., et al. 2010, A&A, 513, L11
- Aerts, C., Mathis, S., & Rogers, T. M. 2019, ARA&A, 57, 35
- Aerts, C., Puls, J., Godart, M., & Dupret, M. A. 2009, A&A, 508, 409
- Aerts, C., Símón-Díaz, S., Bloemen, S., et al. 2017, A&A, 602, A32
- Aerts, C., Símón-Díaz, S., Catala, C., et al. 2013, A&A, 557, A114
- Anders, E. H., Lecoanet, D., Cantiello, M., et al. 2023, Nature Astronomy, 7, 1228

- Bailer-Jones, C. A. L., Rybizki, J., Fousneau, M., Demleitner, M., & Andrae, R. 2021, *AJ*, 161, 147
- Balona, L. A., Baran, A. S., Daszyńska-Daszkiewicz, J., & De Cat, P. 2015, *MNRAS*, 451, 1445
- Bellinger, E. P., de Mink, S. E., van Rossem, W. E., & Justham, S. 2024, *ApJ*, 967, L39
- Blomme, R., Mahy, L., Catala, C., et al. 2011, *A&A*, 533, A4
- Blondin, J. M., Stevens, I. R., & Kallman, T. R. 1991, *ApJ*, 371, 684
- Bowman, D. M. 2020, *Frontiers in Astronomy and Space Sciences*, 7, 70
- Bowman, D. M., Aerts, C., Johnston, C., et al. 2019a, *A&A*, 621, A135
- Bowman, D. M., Burssens, S., Pedersen, M. G., et al. 2019b, *Nature Astronomy*, 3, 760
- Bowman, D. M., Burssens, S., Simón-Díaz, S., et al. 2020, *A&A*, 640, A36
- Bowman, D. M. & Dorn-Wallenstein, T. Z. 2022, *A&A*, 668, A134
- Bowman, D. M., Van Daele, P., Michielsen, M., & Van Reeth, T. 2024, *A&A*, 692, A49
- Brasseur, C. E., Phillip, C., Fleming, S. W., Mullally, S. E., & White, R. L. 2019, *Astrophysics Source Code Library*, record ascl:1905.007
- Bresolin, F., Pietrzyński, G., Urbaneja, M. A., et al. 2006, *ApJ*, 648, 1007
- Brott, I., de Mink, S. E., Cantiello, M., et al. 2011, *A&A*, 530, A115
- Burssens, S., Bowman, D. M., Michielsen, M., et al. 2023, *Nature Astronomy*, 7, 913
- Burssens, S., Simón-Díaz, S., Bowman, D. M., et al. 2020, *A&A*, 639, A81
- Cantiello, M., Langer, N., Brott, I., et al. 2009, *A&A*, 499, 279
- Cantiello, M., Lecoanet, D., Jermyn, A. S., & Grassitelli, L. 2021, *ApJ*, 915, 112
- Cardelli, J. A., Clayton, G. C., & Mathis, J. S. 1989, *ApJ*, 345, 245
- Castro, N., Fossati, L., Langer, N., et al. 2014, *A&A*, 570, L13
- Chesneau, O., Kaufer, A., Stahl, O., et al. 2014, *A&A*, 566, A125
- Cidale, L. S., Haucke, M., Arias, M. L., et al. 2023, *A&A*, 677, A176
- Cutri, R. M., Skrutskie, M. F., van Dyk, S., et al. 2003, *VizieR Online Data Catalog*, II/246
- Cutri, R. M., Wright, E. L., Conrow, T., et al. 2014, *VizieR Online Data Catalog*, II/328
- de Burgos, A., Simón-Díaz, S., Urbaneja, M. A., & Negueruela, I. 2023, *A&A*, 674, A212
- de Mink, S. E., Langer, N., Izzard, R. G., Sana, H., & de Koter, A. 2013, *ApJ*, 764, 166
- Degroote, P., Aerts, C., Baglin, A., et al. 2010, *Nature*, 464, 259
- Degroote, P., Aerts, C., Michel, E., et al. 2012, *A&A*, 542, A88
- Dorn-Wallenstein, T. Z., Levesque, E. M., & Davenport, J. R. A. 2019, *ApJ*, 878, 155
- Dorn-Wallenstein, T. Z., Levesque, E. M., Davenport, J. R. A., et al. 2022, *ApJ*, 940, 27
- Dorn-Wallenstein, T. Z., Levesque, E. M., Neugent, K. F., et al. 2020, *ApJ*, 902, 24
- Edelmann, P. V. F., Ratnasingham, R. P., Pedersen, M. G., et al. 2019, *ApJ*, 876, 4
- Egan, M. P., Price, S. D., Kraemer, K. E., et al. 2003, *VizieR Online Data Catalog*, V/114
- Ekström, S., Georgy, C., Eggenberger, P., et al. 2012, *A&A*, 537, A146
- Farrell, E. J., Groh, J. H., Meynet, G., et al. 2019, *A&A*, 621, A22
- Fraser, M., Dufton, P. L., Hunter, I., & Ryans, R. S. I. 2010, *MNRAS*, 404, 1306
- Gaia Collaboration. 2022, *VizieR Online Data Catalog*, I/355
- Gautschi, A. 2009, *A&A*, 498, 273
- Gebruers, S., Tkachenko, A., Bowman, D. M., et al. 2022, *A&A*, 665, A36
- Georgy, C., Saio, H., & Meynet, G. 2014, *MNRAS*, 439, L6
- Glatzel, W. & Kraus, M. 2024, *MNRAS*, 529, 4947
- Guerrero, N. M., Seager, S., Huang, C. X., et al. 2021, *ApJS*, 254, 39
- Haucke, M., Cidale, L. S., Venero, R. O. J., et al. 2018, *A&A*, 614, A91
- Henneco, J., Schneider, F. R. N., & Laplace, E. 2024, *A&A*, 682, A169
- Howarth, I. D. 2011, *MNRAS*, 413, 1515
- Hubeny, I. & Lanz, T. 1995, *ApJ*, 439, 875
- Ishihara, D., Onaka, T., Kataza, H., et al. 2010, *A&A*, 514, A1
- Jermyn, A. S., Anders, E. H., & Cantiello, M. 2022, *ApJ*, 926, 221
- Jones, C. & Liller, W. 1973, *ApJ*, 184, L121
- Kaufer, A., Stahl, O., Prinja, R. K., & Witherick, D. 2006, *A&A*, 447, 325
- Kaufer, A., Stahl, O., Tubbesing, S., et al. 1999, *The Messenger*, 95, 8
- Kaufer, A., Stahl, O., Wolf, B., et al. 1997, *A&A*, 320, 273
- Klencki, J., Istrate, A., Nelemans, G., & Pols, O. 2022, *A&A*, 662, A56
- Kourmliotis, M., Bonanos, A. Z., Williams, S. J., et al. 2015, *A&A*, 582, A42
- Kourmliotis, M., Kraus, M., Maryeva, O., Borges Fernandes, M., & Maravelias, G. 2022, *MNRAS*, 511, 4360
- Kraus, M., Haucke, M., Cidale, L. S., et al. 2015, *A&A*, 581, A75
- Kraus, M., Kourmliotis, M., Arias, M. L., Torres, A. F., & Nickeler, D. H. 2023, *Galaxies*, 11, 76
- Krtićka, J. & Feldmeier, A. 2021, *A&A*, 648, A79
- Krtićka, J., Kubát, J., & Krtićková, I. 2021, *A&A*, 647, A28
- Kudritzki, R.-P., Urbaneja, M. A., Gazak, Z., et al. 2012, *ApJ*, 747, 15
- Kuszelewicz, J. S., Hekker, S., & Bell, K. J. 2020, *MNRAS*, 497, 4843
- Labadie-Bartz, J., Carciofi, A. C., Henrique de Amorim, T., et al. 2022, *AJ*, 163, 226
- Langer, N. & Kudritzki, R. P. 2014, *A&A*, 564, A52
- Lanz, T. & Hubeny, I. 2007, *ApJS*, 169, 83
- Lecoanet, D., Cantiello, M., Quataert, E., et al. 2019, *ApJ*, 886, L15
- Lefever, K., Puls, J., & Aerts, C. 2007, *A&A*, 463, 1093
- Lefèvre, L., Marchenko, S. V., Moffat, A. F. J., & Acker, A. 2009, *A&A*, 507, 1141
- Lightkurve Collaboration, Cardoso, J. V. d. M., Hedges, C., et al. 2018, *Astrophysics Source Code Library*, record ascl:1812.013
- Ma, L., Johnston, C., Bellinger, E. P., & de Mink, S. E. 2024, *ApJ*, 966, 196
- Maeder, A. 1980, *A&A*, 90, 311
- Maeder, A. & Ruffener, F. 1972, *A&A*, 20, 437
- Martinet, S., Meynet, G., Ekström, S., et al. 2021, *A&A*, 648, A126
- Menon, A., Ercolino, A., Urbaneja, M. A., et al. 2024, *ApJ*, 963, L42
- Mermilliod, J. C. 2006, *VizieR Online Data Catalog*, II/168
- Meynet, G., Chomienne, V., Ekström, S., et al. 2015, *A&A*, 575, A60
- Morel, T., Marchenko, S. V., Pati, A. K., et al. 2004, *MNRAS*, 351, 552
- Nazé, Y., Rauw, G., & Gosset, E. 2021, *MNRAS*, 502, 5038
- Oudmaijer, R. D., Davies, B., de Wit, W. J., & Patel, M. 2009, *ASPC*, 412, 17
- Paegert, M., Stassun, K. G., Collins, K. A., et al. 2021, *arXiv:2108.04778*
- Pedersen, M. G., Chowdhury, S., Johnston, C., et al. 2019, *ApJ*, 872, L9
- Quaintrell, H., Norton, A. J., Ash, T. D. C., et al. 2003, *A&A*, 401, 313
- Ratnasingham, R. P., Rogers, T. M., Chowdhury, S., et al. 2023, *A&A*, 674, A134
- Ricker, G. R., Winn, J. N., Vanderspek, R., et al. 2015, *J. Astron. Tel. Instr. Syst.*, 1, 014003
- Rogers, T. M., Lin, D. N. C., McElwaine, J. N., & Lau, H. H. B. 2013, *ApJ*, 772, 21
- Saio, H. 2011, *MNRAS*, 412, 1814
- Saio, H., Georgy, C., & Meynet, G. 2013, *MNRAS*, 433, 1246
- Saio, H., Kuschnig, R., Gautschi, A., et al. 2006, *ApJ*, 650, 1111
- Salmon, S. J. A. J., Montalbán, J., Reese, D. R., Dupret, M. A., & Eggenberger, P. 2014, *A&A*, 569, A18
- Samus, N. N., Kazarovets, E. V., Durlevich, O. V., Kireeva, N. N., & Pastukhova, E. N. 2017, *Astronomy Reports*, 61, 80
- Sanders, J. L. & Das, P. 2018, *MNRAS*, 481, 4093
- Schultz, W. C., Bildsten, L., & Jiang, Y.-F. 2022, *ApJ*, 924, L11
- Shen, D.-X., Zhu, C.-H., Lü, G.-L., Lu, X.-z., & He, X.-l. 2024, *ApJS*, 275, 2
- Shiode, J. H., Quataert, E., Cantiello, M., & Bildsten, L. 2013, *MNRAS*, 430, 1736
- Simón-Díaz, S., Aerts, C., Urbaneja, M. A., et al. 2018, *A&A*, 612, A40
- Simón-Díaz, S., Herrero, A., Uytterhoeven, K., et al. 2010, *ApJ*, 720, L174
- Southworth, J., Bowman, D. M., Tkachenko, A., & Pavlovski, K. 2020, *MNRAS*, 497, L19
- Spejcher, B., Richardson, N. D., Pablo, H., et al. 2025, *AJ*, 169, 128
- Stanishev, V., Kraicheva, Z., Boffin, H. M. J., & Genkov, V. 2002, *A&A*, 394, 625
- Thompson, W., Herwig, F., Woodward, P. R., et al. 2024, *MNRAS*, 531, 1316
- Urbaneja, M. A., Kudritzki, R.-P., Bresolin, F., et al. 2008, *ApJ*, 684, 118
- Vanderspek, R., Doty, J., Fausnaugh, M., et al. 2018, *TESS Instrument Handbook*
- Vanon, R., Edelmann, P. V. F., Ratnasingham, R. P., Varghese, A., & Rogers, T. M. 2023, *ApJ*, 954, 171
- Virtanen, P., Gommers, R., Oliphant, T. E., et al. 2020, *Nature Methods*, 17, 261
- Yoon, S.-C. & Cantiello, M. 2010, *ApJ*, 717, L62
- Zacharias, N., Monet, D. G., Levine, S. E., et al. 2004, in *AAS Meet. Abs.*, Vol. 205, 48.15

## Appendix A: Supplementary tables

**Table A.1.** List of the 41 studied BSGs in the Galaxy. Coordinates and spectral types are taken from Simbad. The last four columns contain a log of the TESS observations, including the crowding metric for the adopted aperture.

#	Star	RA [deg]	DEC [deg]	Sp. type	TIC	$T$ [mag]	CROWDSAP <sup>(+)</sup>	TESS sectors
01	HD 51309	104.034250	-17.054239	B3Ib	146908355	4.5	0.999	6,7,33
02	HD 64760	118.325625	-48.102933	B0.5Ib	269064487	4.4	0.983	7,8,9,34,35,61,62
03	HD 74371 <sup>a</sup>	130.487083	-45.410711	B6Iab/b	285823086	5.0	0.994	8,9,35,36,61,62
04	HD 75149	131.627250	-45.912506	B5Iab	28656140	5.2	0.996	8,9,35,36,62
05	HD 77581 <sup>a,b</sup>	135.528583	-40.554694	B0.5Ia	191450569	6.5	0.992	8,9,62
06	HD 79186	137.768333	-44.867903	B5Ia	74533697	4.8	0.891	8,9,35,36,62,63
07	HD 80558 <sup>a</sup>	139.676458	-51.560650	B6Ia	364151367	5.3	0.996	9,10,35,36,62,63
08	HD 83183	143.611042	-59.229753	B5II	439431474	4.1	0.997	10,36,62,63,64
09	HD 91619 <sup>a</sup>	158.355792	-58.190147	B6Iab	457803940	5.6	0.994	10,36,37,63,64
10	HD 92964	160.669042	-59.215758	B2.5Ia	458704469	5.2	0.987	10,36,37,63,64
11	HD 93840	162.286208	-46.778286	B1/2Iab/b	147215618	7.9	0.981	10,36,37,63
12	HD 94493	163.312917	-60.814778	B0.5Iab/b	465384125	7.3	0.938	10,11,63,64
13	HD 96248	166.239875	-59.858903	B1Iab	305919188	6.3	0.986	10,11,63,64
14	HD 99857	172.113292	-66.489275	B1Ib	296059122	7.4	0.986	10,11,37,38,64
15	HD 99953 <sup>a</sup>	172.313167	-63.553936	B2Ia	317046099	4.8	0.998	10,11,37,38,64
16	HD 103779	179.239792	-63.249089	B0.5II	306562451	7.4	0.963	10,11,37,38
17	HD 105071	181.473417	-65.546875	B8Ia	379870355	6.1	0.990	11,37,38,64,65
18	HD 106343 <sup>a</sup>	183.570542	-64.408519	B1.5Ia	382515892	6.3	0.980	11,37,38,64,65
19	HD 108002	186.233167	-65.211014	B2Ia/ab	450383399	6.8	0.980	11,37,38
20	HD 109867	189.718167	-67.193050	B0.5/1Iab	327774344	6.2	0.957	11,38,64,65
21	HD 111558	192.799833	-69.645208	B7Ib	333977706	7.1	0.981	11,12,38,64
22	HD 111973 <sup>b</sup>	193.453792	-60.376239	B5I	436267716	5.8	0.764	11,37,38,64,65
23	HD 115842	200.201417	-55.800689	B0.5Ia	256813340	5.8	0.992	11,38,64
24	HD 116084	200.567875	-52.182953	B2Ib	401431637	5.7	0.998	11,38,64
25	HD 117024	202.272583	-63.874031	B2Ib	314141881	7.2	0.942	11
26	HD 119646	206.575000	-62.451600	B1.5Ib	323082858	5.3	0.996	11,38,65
27	HD 122879	211.604833	-59.715903	B0Ia	210096523	5.3	0.990	11,38
28	HD 125288	215.081417	-56.386494	B5II	413632344	4.1	0.992	11,38,65
29	HD 125545	215.512583	-58.291214	B1Iab/b	413965764	6.2	0.998	11,38
30	HD 141318	237.778333	-55.055536	B2III	80724706	5.9	0.842	12,39,65
31	HD 142758	239.848917	-58.726222	B1Ia	422192335	6.9	0.925	12,39
32	HD 148379 <sup>a</sup>	247.426375	-46.243231	B2Iab	226037847	4.8	0.994	12,39,66
33	HD 148688 <sup>a</sup>	247.924042	-41.817147	B1Iaeqp	29563900	4.9	0.955	12,39,66
34	HD 149038	248.520917	-44.045314	O9.7Iab	228529130	4.9	0.987	39,66
35	HD 150168	250.417625	-49.651553	B1Iab/Ib	39177520	5.7	0.983	12,39,66
36	HD 150898	251.831917	-58.341442	B0Ib	344237828	5.7	0.995	12,39,66
37	HD 152234 <sup>b</sup>	253.507667	-41.806392	B0.5Ia	339565401	5.2	0.481	12,39,66
38	HD 152235	253.495208	-41.994328	B0.5Ia	246957312	4.3	0.997	39
39	HD 154090	256.205625	-34.122928	B2Iab	41026067	4.6	0.991	12,39,66
40	HD 155985	259.273083	-44.778594	B0.5Ib	216802672	6.2	0.993	12,39
41	HD 157038 <sup>a</sup>	260.663417	-37.804639	B3Iap	198257590	4.4	0.991	39,66

**Notes.** <sup>(a)</sup> Star identified as an  $\alpha$  Cygni variable (Lefèvre et al. 2009; Samus et al. 2017). <sup>(b)</sup> Reported in Simbad as a binary/multiple system.

**Table A.2.** Statistical measures of the TESS light curves and parameters of the SLF variability. Uncertainties are given in parentheses. The middle column contains a flag that indicates when a star is a candidate rotating (cROT) variable.

Star	$\sigma$ [mag]	$\psi^2$	skw	cROT	$\log(\alpha_w$ [mag])	$\log(\alpha_0$ [mag])	$\tau$ [d]	$\gamma$
HD 51309	0.007 (0.001)	1.67 (0.15)	0.03 (0.66)	Y	-5.147 (0.011)	-3.860 (0.004)	0.055 (0.001)	4.125 (0.125)
HD 64760	0.006 (0.001)	1.54 (0.06)	-0.13 (0.06)	Y	-5.642 (0.017)	-3.153 (0.001)	0.076 (<0.001)	2.124 (0.011)
HD 74371	0.009 (0.002)	1.84 (0.07)	0.22 (0.34)	N	-5.514 (0.003)	-3.720 (0.001)	0.126 (0.001)	1.867 (0.009)
HD 75149	0.011 (0.003)	1.91 (0.05)	0.17 (0.26)	N	-5.169 (0.003)	-3.654 (0.002)	0.092 (<0.001)	5.256 (0.079)
HD 77581	0.031 (0.002)	1.72 (0.16)	-0.07 (0.10)	Y	-5.192 (0.010)	-3.439 (0.002)	0.065 (<0.001)	5.927 (0.126)
HD 79186	0.010 (0.002)	2.04 (0.06)	0.34 (0.18)	N	-5.299 (0.004)	-3.106 (0.001)	0.252 (0.001)	1.579 (0.007)
HD 80558	0.010 (0.002)	2.19 (0.43)	0.26 (0.25)	N	-4.882 (0.031)	-3.493 (0.009)	0.222 (0.009)	1.237 (0.036)
HD 83183	0.002 (0.001)	1.53 (0.33)	0.11 (0.18)	Y	-5.790 (0.011)	-3.673 (0.002)	0.073 (<0.001)	2.990 (0.029)
HD 91619	0.013 (0.003)	1.93 (0.26)	0.11 (0.12)	N	-5.207 (0.016)	-4.311 (0.010)	0.086 (0.003)	2.596 (0.139)
HD 92964	0.014 (0.002)	1.71 (0.16)	-0.08 (0.35)	N	-4.607 (0.021)	-3.690 (0.012)	0.091 (0.004)	1.927 (0.102)
HD 93840	0.011 (0.002)	1.77 (0.15)	0.03 (0.05)	Y	-4.352 (0.024)	-2.937 (0.005)	0.114 (0.002)	2.449 (0.068)
HD 94493	0.006 (0.001)	1.59 (0.15)	-0.41 (0.20)	Y	-4.685 (0.033)	-3.237 (0.006)	0.092 (0.002)	2.308 (0.069)
HD 96248	0.015 (0.002)	3.02 (1.11)	0.24 (0.27)	Y	-4.308 (0.014)	-3.088 (0.005)	0.127 (0.002)	3.962 (0.144)
HD 99857	0.005 (0.000)	1.63 (0.07)	-0.17 (0.06)	Y	-5.115 (0.012)	-3.110 (0.002)	0.082 (0.001)	2.178 (0.022)
HD 99953	0.014 (0.002)	2.16 (0.74)	0.23 (0.10)	Y	-5.255 (0.005)	-3.751 (0.003)	0.074 (<0.001)	3.798 (0.068)
HD 103779	0.007 (<0.001)	1.62 (0.28)	-0.11 (0.08)	Y	-4.491 (0.022)	-3.229 (0.005)	0.070 (0.001)	2.925 (0.091)
HD 105071	0.007 (<0.001)	1.99 (0.47)	0.10 (0.22)	N	-4.751 (0.016)	-3.585 (0.006)	0.127 (0.002)	6.222 (0.383)
HD 106343	0.014 (0.002)	2.28 (0.46)	0.09 (0.37)	Y	-4.312 (0.017)	-3.161 (0.006)	0.103 (0.002)	4.418 (0.216)
HD 108002	0.011 (0.002)	1.83 (<0.01)	-0.05 (0.24)	Y	-4.206 (0.023)	-2.899 (0.007)	0.125 (0.002)	3.631 (0.175)
HD 109867	0.012 (0.001)	2.24 (0.42)	-0.22 (0.50)	Y	-4.472 (0.015)	-3.533 (0.007)	0.062 (0.001)	5.542 (0.334)
HD 111558	0.008 (0.001)	1.94 (0.35)	-0.40 (0.31)	N	-5.007 (0.009)	-3.718 (0.005)	0.104 (0.001)	3.131 (0.090)
HD 111973	0.010 (0.003)	1.91 (0.10)	0.05 (0.05)	N	-5.229 (0.005)	-3.662 (0.002)	0.041 (<0.001)	2.541 (0.026)
HD 115842	0.016 (0.003)	1.75 (0.03)	-0.31 (0.40)	Y	-5.506 (0.008)	-3.579 (0.002)	0.054 (<0.001)	3.576 (0.040)
HD 116084	0.011 (0.001)	1.80 (0.11)	-0.45 (0.17)	Y	-5.500 (0.007)	-3.629 (0.002)	0.072 (<0.001)	4.095 (0.052)
HD 117024 <sup>a</sup>	0.003	1.58	-0.33	Y	-4.630 (0.025)	-3.458 (0.007)	0.066 (0.001)	3.747 (0.184)
HD 119646	0.009 (0.001)	1.78 (0.31)	-0.21 (0.16)	Y	-4.384 (0.025)	-3.070 (0.008)	0.121 (0.003)	2.250 (0.082)
HD 122879	0.009 (0.003)	2.08 (0.31)	-0.18 (0.22)	N	-5.343 (0.013)	-3.102 (0.001)	0.082 (<0.001)	4.269 (0.049)
HD 125288	0.002 (0.001)	1.44 (0.22)	-0.69 (0.57)	Y	-5.244 (0.007)	-4.192 (0.004)	0.051 (<0.001)	5.629 (0.202)
HD 125545	0.011 (<0.001)	1.60 (0.32)	0.02 (0.26)	Y	-4.476 (0.030)	-3.192 (0.007)	0.073 (0.001)	3.206 (0.142)
HD 141318	0.001 (<0.001)	1.34 (0.07)	-0.46 (0.10)	Y	-5.584 (0.004)	-4.013 (0.002)	0.050 (<0.001)	1.827 (0.015)
HD 142758	0.013 (0.003)	2.40 (0.95)	-0.32 (0.28)	N	-4.529 (0.016)	-3.478 (0.006)	0.088 (0.001)	5.411 (0.317)
HD 148379	0.016 (0.006)	1.89 (0.03)	0.10 (0.35)	N	-5.400 (0.003)	-3.751 (0.002)	0.118 (0.001)	1.596 (0.011)
HD 148688	0.012 (0.001)	1.98 (0.09)	-0.09 (0.28)	N	-5.096 (0.002)	-3.609 (0.002)	0.106 (0.001)	2.604 (0.026)
HD 149038	0.010 (0.002)	1.61 (<0.01)	0.17 (0.16)	Y	-5.238 (0.011)	-3.098 (0.001)	0.064 (<0.001)	3.022 (0.026)
HD 150168	0.007 (0.001)	1.73 (0.05)	-0.44 (0.16)	Y	-5.319 (0.015)	-3.093 (0.002)	0.074 (0.001)	2.029 (0.017)
HD 150898	0.006 (0.001)	1.58 (0.08)	0.00 (0.18)	Y	-5.339 (0.012)	-3.112 (0.002)	0.066 (<0.001)	2.297 (0.016)
HD 152234	0.009 (0.002)	1.70 (0.20)	-0.24 (0.44)	Y	-5.018 (0.020)	-3.347 (0.004)	0.077 (0.001)	3.214 (0.076)
HD 152235 <sup>a</sup>	0.014	1.92	0.21	N	-5.312 (0.004)	-3.698 (0.002)	0.063 (<0.001)	3.280 (0.034)
HD 154090	0.014 (0.004)	1.74 (0.16)	-0.07 (0.09)	Y	-5.245 (0.006)	-3.478 (0.002)	0.065 (<0.001)	4.483 (0.058)
HD 155985	0.006 (0.001)	1.54 (0.13)	0.08 (0.32)	Y	-4.399 (0.024)	-3.294 (0.007)	0.060 (0.001)	3.468 (0.166)
HD 157038	0.010 (0.001)	1.79 (0.14)	-0.13 (0.14)	N	-5.417 (0.002)	-3.922 (0.002)	0.083 (<0.001)	2.621 (0.023)

Notes. <sup>(a)</sup> Data studied from a single TESS sector.

**Table A.3.** Eddington factors  $\Gamma_e$  and SED-based scaling factors  $C$  of the sample BSGs. The last two columns contain luminosities and the absolute  $G$ -band magnitudes, which were calculated using the distance values from *Gaia* (third column).

Star	$\Gamma_e$	$D_{Gaia}$ [pc]	$\log C$	$\log (L/L_{\odot})$	$M_G$ [mag]
HD 51309	0.18	1108 <sup>+408</sup> <sub>-214</sub>	-1.49	4.84 <sup>+0.27</sup> <sub>-0.19</sub>	-6.06 <sup>-0.68</sup> <sub>+0.47</sub>
HD 64760	0.19	659 <sup>+58</sup> <sub>-53</sub>	-1.67	4.91 <sup>+0.07</sup> <sub>-0.07</sub>	-5.17 <sup>-0.19</sup> <sub>+0.18</sub>
HD 74371	0.31	1718 <sup>+177</sup> <sub>-141</sub>	-1.43	5.07 <sup>+0.09</sup> <sub>-0.07</sub>	-6.87 <sup>-0.21</sup> <sub>+0.19</sub>
HD 75149	0.31	1466 <sup>+121</sup> <sub>-123</sub>	-1.47	5.16 <sup>+0.06</sup> <sub>-0.09</sub>	-6.58 <sup>-0.17</sup> <sub>+0.19</sub>
HD 77581	0.47	1969 <sup>+61</sup> <sub>-68</sub>	-1.79	5.66 <sup>+0.02</sup> <sub>-0.04</sub>	-6.51 <sup>-0.07</sup> <sub>+0.08</sub>
HD 79186	0.39	1677 <sup>+212</sup> <sub>-201</sub>	-1.41	5.29 <sup>+0.11</sup> <sub>-0.10</sub>	-7.14 <sup>-0.26</sup> <sub>+0.28</sub>
HD 80558	0.43	1862 <sup>+80</sup> <sub>-90</sub>	-1.34	5.27 <sup>+0.03</sup> <sub>-0.04</sub>	-7.27 <sup>-0.09</sup> <sub>+0.11</sub>
HD 83183	0.12	593 <sup>+55</sup> <sub>-56</sub>	-1.38	4.44 <sup>+0.07</sup> <sub>-0.09</sub>	-5.16 <sup>-0.19</sup> <sub>+0.21</sub>
HD 91619	0.44	2319 <sup>+144</sup> <sub>-100</sub>	-1.48	5.18 <sup>+0.06</sup> <sub>-0.03</sub>	-7.10 <sup>-0.13</sup> <sub>+0.10</sub>
HD 92964	0.45	2130 <sup>+288</sup> <sub>-238</sub>	-1.44	5.50 <sup>+0.11</sup> <sub>-0.10</sub>	-7.46 <sup>-0.28</sup> <sub>+0.26</sub>
HD 93840	0.26	2649 <sup>+241</sup> <sub>-231</sub>	-2.22	4.64 <sup>+0.08</sup> <sub>-0.08</sub>	-4.82 <sup>-0.19</sup> <sub>+0.20</sub>
HD 94493	0.26	2167 <sup>+109</sup> <sub>-94</sub>	-2.13	4.85 <sup>+0.04</sup> <sub>-0.04</sub>	-5.11 <sup>-0.11</sup> <sub>+0.10</sub>
HD 96248	0.44	2426 <sup>+122</sup> <sub>-113</sub>	-1.81	5.27 <sup>+0.04</sup> <sub>-0.05</sub>	-6.43 <sup>-0.11</sup> <sub>+0.10</sub>
HD 99857	0.18	1794 <sup>+75</sup> <sub>-57</sub>	-2.08	4.63 <sup>+0.04</sup> <sub>-0.03</sub>	-4.75 <sup>-0.09</sup> <sub>+0.07</sub>
HD 99953	0.43	2490 <sup>+165</sup> <sub>-127</sub>	-1.64	5.37 <sup>+0.05</sup> <sub>-0.05</sub>	-6.90 <sup>-0.14</sup> <sub>+0.11</sub>
HD 103779	0.30	2039 <sup>+134</sup> <sub>-96</sub>	-2.13	4.90 <sup>+0.06</sup> <sub>-0.04</sub>	-5.05 <sup>-0.14</sup> <sub>+0.10</sub>
HD 105071	0.24	2187 <sup>+96</sup> <sub>-94</sub>	-1.62	4.73 <sup>+0.05</sup> <sub>-0.03</sub>	-6.24 <sup>-0.09</sup> <sub>+0.10</sub>
HD 106343	0.39	2379 <sup>+144</sup> <sub>-125</sub>	-1.81	5.30 <sup>+0.05</sup> <sub>-0.05</sub>	-6.51 <sup>-0.13</sup> <sub>+0.12</sub>
HD 108002	0.32	2391 <sup>+103</sup> <sub>-93</sub>	-1.93	5.07 <sup>+0.04</sup> <sub>-0.03</sub>	-5.88 <sup>-0.09</sup> <sub>+0.09</sub>
HD 109867	0.33	2552 <sup>+219</sup> <sub>-172</sub>	-1.86	5.43 <sup>+0.08</sup> <sub>-0.05</sub>	-6.56 <sup>-0.18</sup> <sub>+0.15</sub>
HD 111558	0.16	4594 <sup>+589</sup> <sub>-516</sub>	-1.86	4.90 <sup>+0.09</sup> <sub>-0.12</sub>	-6.69 <sup>-0.26</sup> <sub>+0.26</sub>
HD 111973	0.25	1948 <sup>+203</sup> <sub>-151</sub>	-1.6	5.15 <sup>+0.08</sup> <sub>-0.07</sub>	-6.57 <sup>-0.21</sup> <sub>+0.17</sub>
HD 115842	0.51	1682 <sup>+84</sup> <sub>-91</sub>	-1.71	5.57 <sup>+0.03</sup> <sub>-0.06</sub>	-6.53 <sup>-0.11</sup> <sub>+0.12</sub>
HD 116084	0.29	1958 <sup>+161</sup> <sub>-147</sub>	-1.67	5.04 <sup>+0.06</sup> <sub>-0.07</sub>	-6.36 <sup>-0.17</sup> <sub>+0.17</sub>
HD 117024	0.16	1984 <sup>+84</sup> <sub>-92</sub>	-1.98	4.47 <sup>+0.02</sup> <sub>-0.05</sub>	-4.96 <sup>-0.09</sup> <sub>+0.10</sub>
HD 119646	0.23	1721 <sup>+84</sup> <sub>-73</sub>	-1.84	4.73 <sup>+0.04</sup> <sub>-0.04</sub>	-5.40 <sup>-0.10</sup> <sub>+0.09</sub>
HD 122879	0.52	2274 <sup>+179</sup> <sub>-195</sub>	-1.91	5.59 <sup>+0.06</sup> <sub>-0.08</sub>	-6.44 <sup>-0.16</sup> <sub>+0.20</sub>
HD 125288	0.08	438 <sup>+51</sup> <sub>-30</sub>	-1.34	4.13 <sup>+0.09</sup> <sub>-0.06</sub>	-4.50 <sup>-0.24</sup> <sub>+0.16</sub>
HD 125545	0.25	2171 <sup>+84</sup> <sub>-89</sub>	-2.01	4.87 <sup>+0.04</sup> <sub>-0.03</sub>	-5.29 <sup>-0.08</sup> <sub>+0.09</sub>
HD 141318	0.11	596 <sup>+14</sup> <sub>-19</sub>	-1.73	4.09 <sup>+0.02</sup> <sub>-0.02</sub>	-3.71 <sup>-0.05</sup> <sub>+0.07</sub>
HD 142758	0.38	3156 <sup>+172</sup> <sub>-161</sub>	-1.86	5.19 <sup>+0.04</sup> <sub>-0.05</sub>	-6.49 <sup>-0.12</sup> <sub>+0.11</sub>
HD 148379	0.63	1585 <sup>+204</sup> <sub>-168</sub>	-1.29	5.70 <sup>+0.10</sup> <sub>-0.10</sub>	-7.66 <sup>-0.26</sup> <sub>+0.24</sub>
HD 148688	0.49	1348 <sup>+215</sup> <sub>-154</sub>	-1.44	5.60 <sup>+0.12</sup> <sub>-0.11</sub>	-6.97 <sup>-0.32</sup> <sub>+0.26</sub>
HD 149038	0.40	896 <sup>+91</sup> <sub>-84</sub>	-1.67	5.33 <sup>+0.09</sup> <sub>-0.08</sub>	-5.75 <sup>-0.21</sup> <sub>+0.21</sub>
HD 150168	0.20	1015 <sup>+75</sup> <sub>-66</sub>	-1.8	4.94 <sup>+0.07</sup> <sub>-0.05</sub>	-5.54 <sup>-0.15</sup> <sub>+0.15</sub>
HD 150898	0.29	1118 <sup>+112</sup> <sub>-83</sub>	-1.87	4.99 <sup>+0.09</sup> <sub>-0.06</sub>	-5.22 <sup>-0.21</sup> <sub>+0.17</sub>
HD 152234	0.42	1935 <sup>+586</sup> <sub>-575</sub>	-1.65	5.86 <sup>+0.24</sup> <sub>-0.30</sub>	-7.16 <sup>-0.57</sup> <sub>+0.77</sub>
HD 152235	0.40	1618 <sup>+133</sup> <sub>-94</sub>	-1.6	5.55 <sup>+0.06</sup> <sub>-0.06</sub>	-6.73 <sup>-0.17</sup> <sub>+0.13</sub>
HD 154090	0.37	1116 <sup>+131</sup> <sub>-137</sub>	-1.45	5.54 <sup>+0.09</sup> <sub>-0.12</sub>	-6.76 <sup>-0.24</sup> <sub>+0.28</sub>
HD 155985	0.25	1077 <sup>+38</sup> <sub>-35</sub>	-1.83	4.82 <sup>+0.03</sup> <sub>-0.03</sub>	-4.96 <sup>-0.08</sup> <sub>+0.07</sub>
HD 157038	0.46	2168 <sup>+134</sup> <sub>-102</sub>	-1.34	5.74 <sup>+0.04</sup> <sub>-0.05</sub>	-7.89 <sup>-0.13</sup> <sub>+0.10</sub>



## **Appendix B: Supplementary figures.**

In this section, we provide supplementary figures following the Figs. 1, 3, and 4.

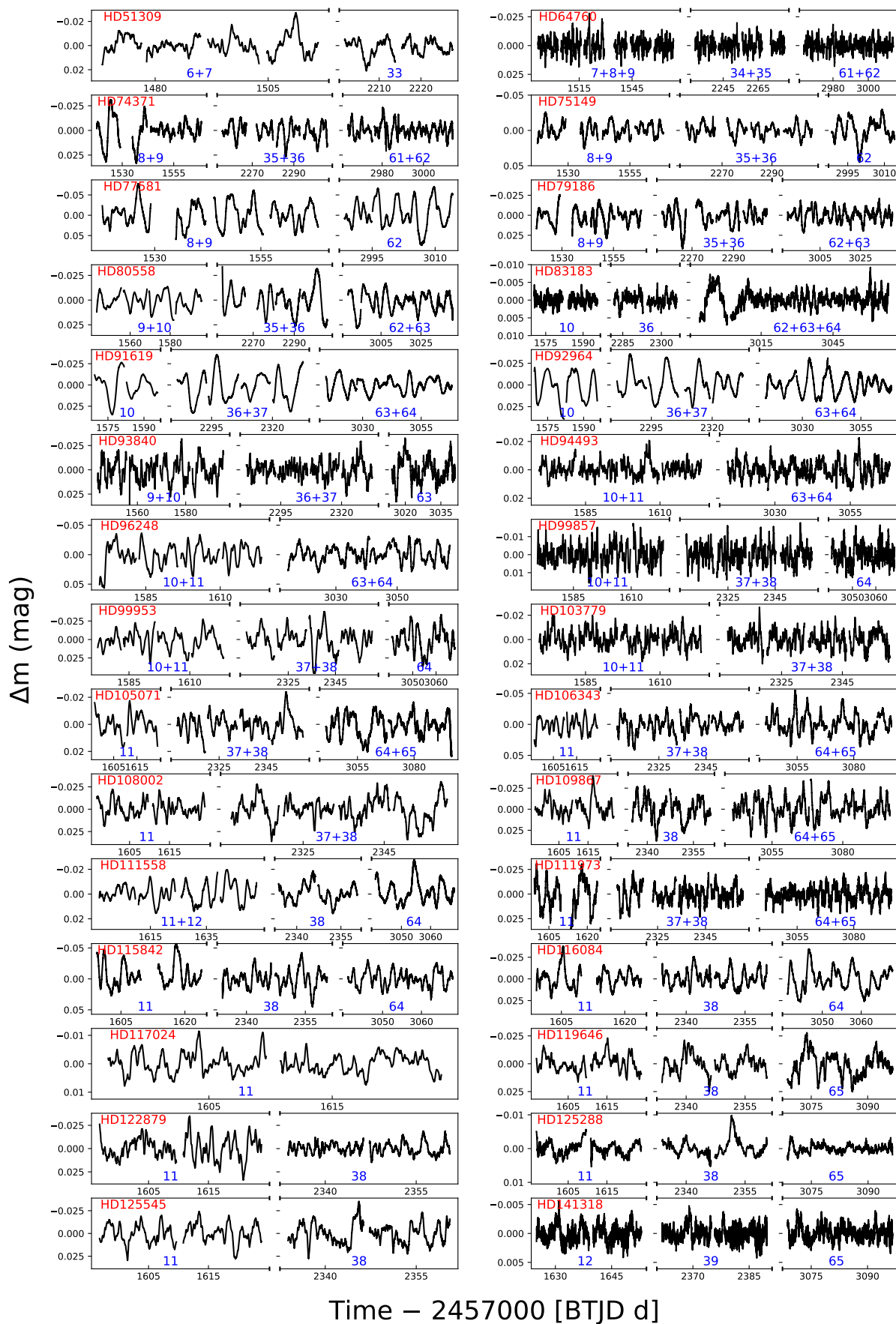


**Fig. B.1.** TESS photometry as in Fig. 1, for the stars 1 – 30 from Table A.1.

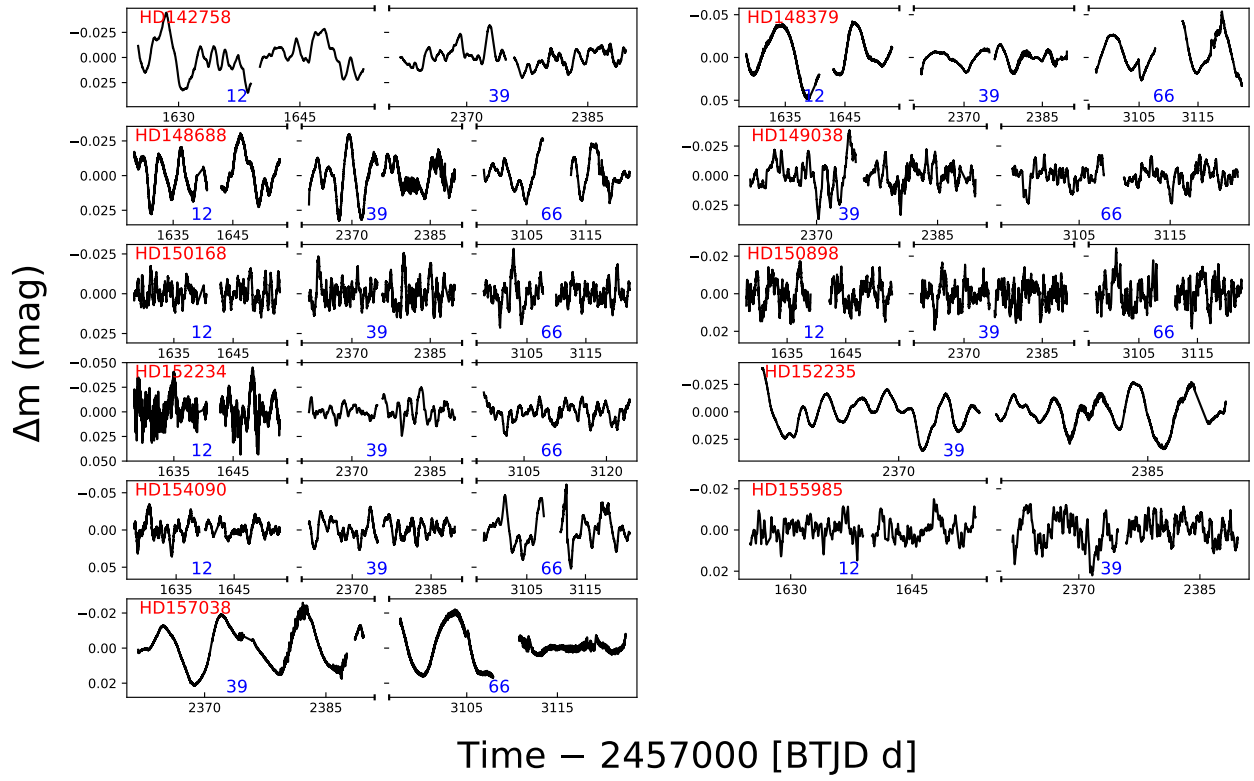


**Fig. B.2.** TESS photometry as in Fig. 1, for the stars 31 – 41 from Table A.1.

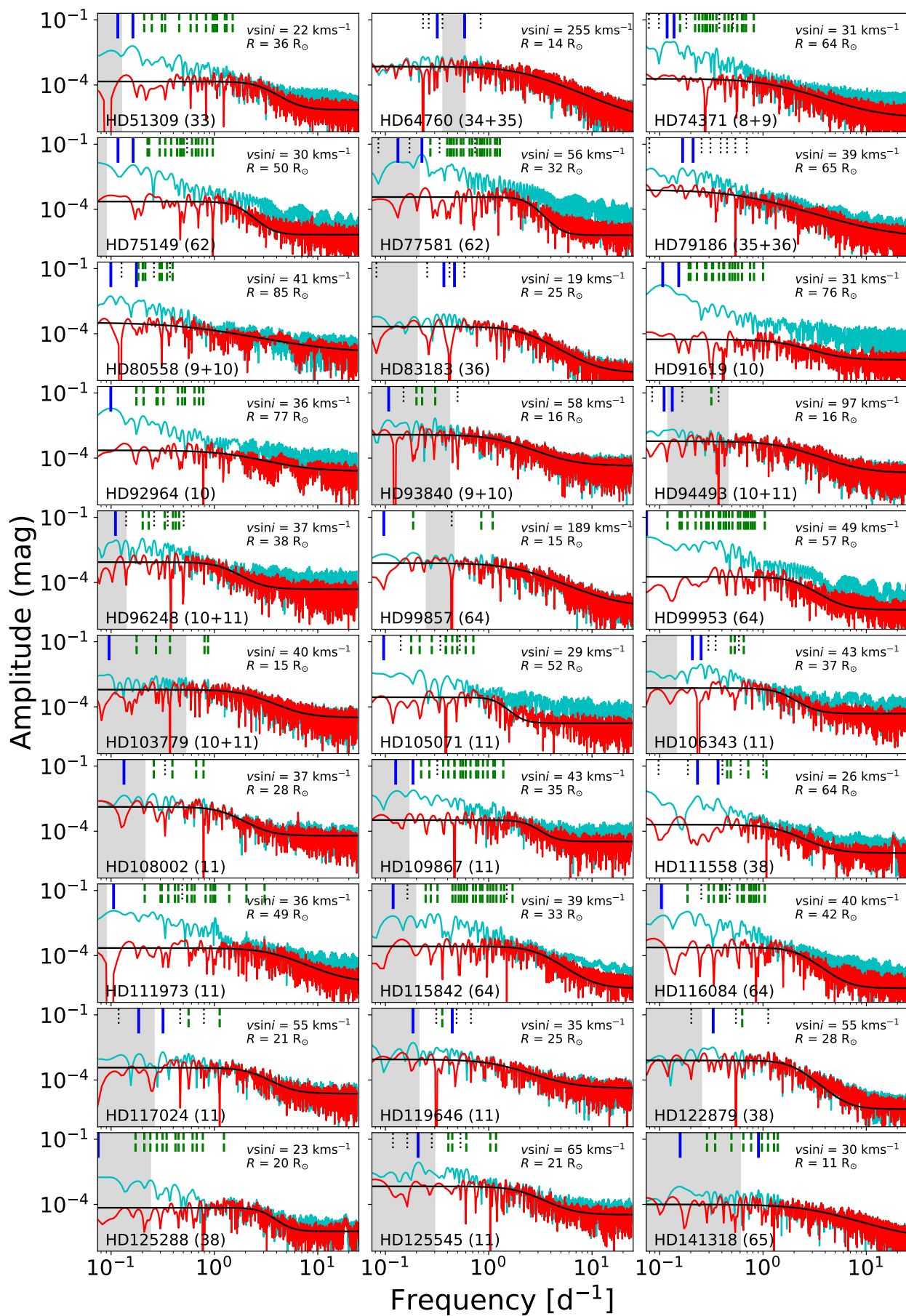


**Fig. B.3.** Frequency spectra as in Fig. 3, for the stars 1 – 30 from Table A.1.

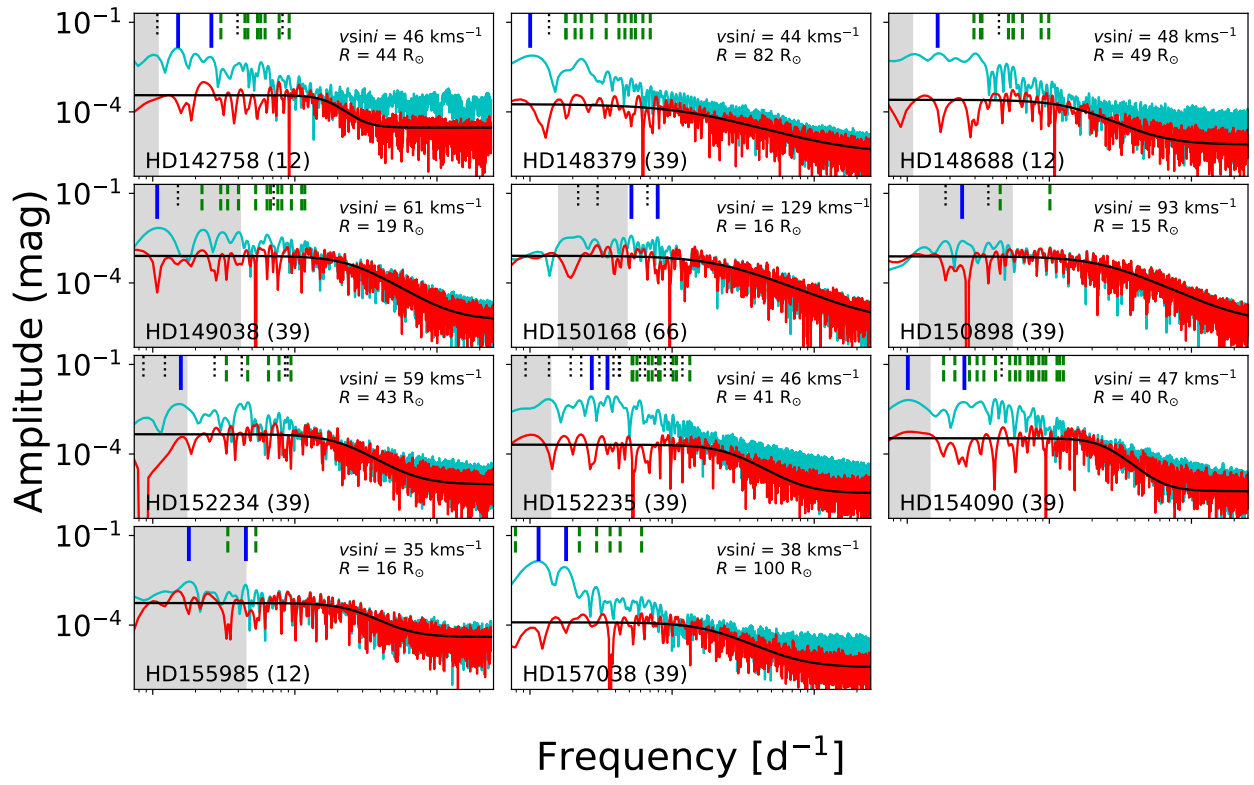
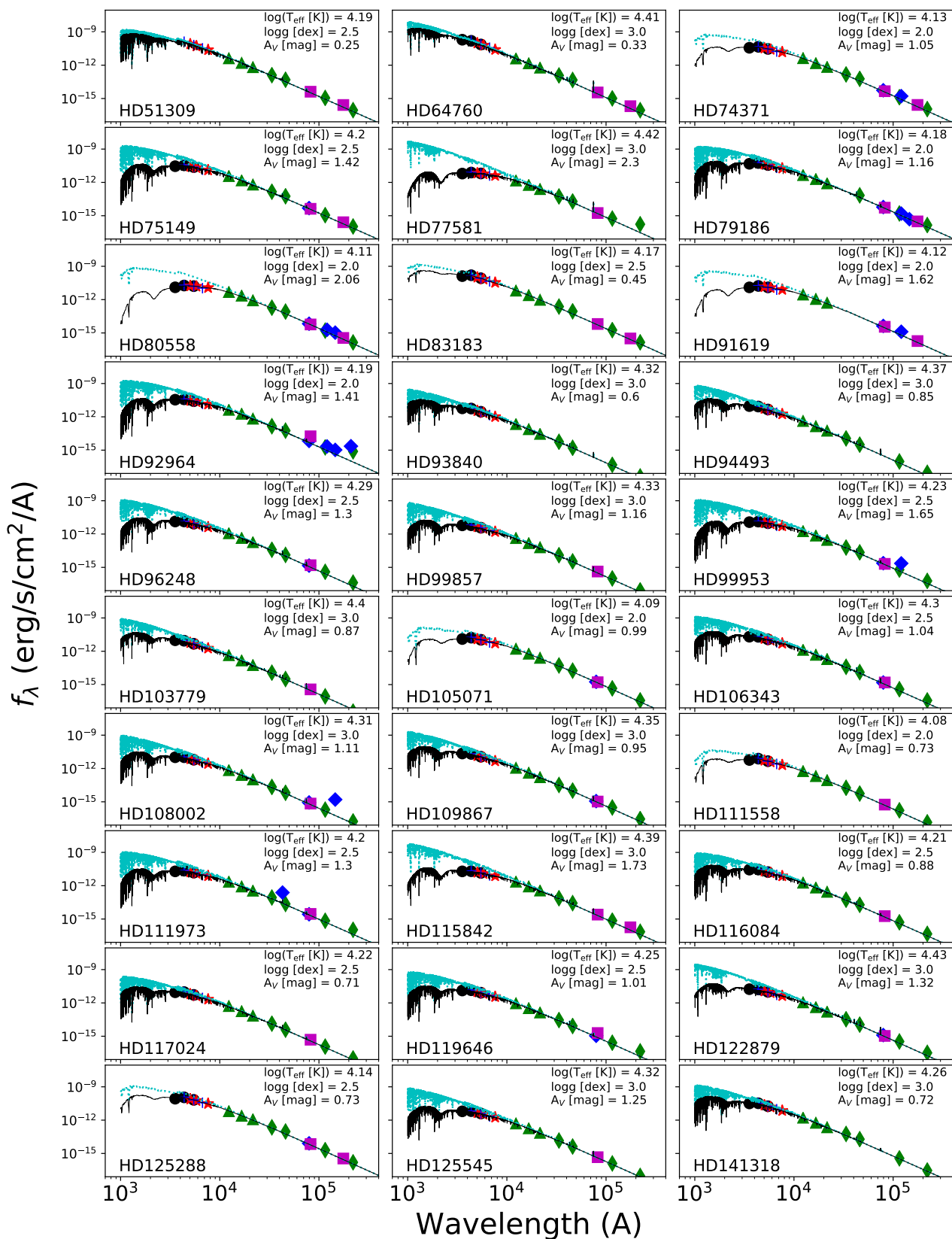
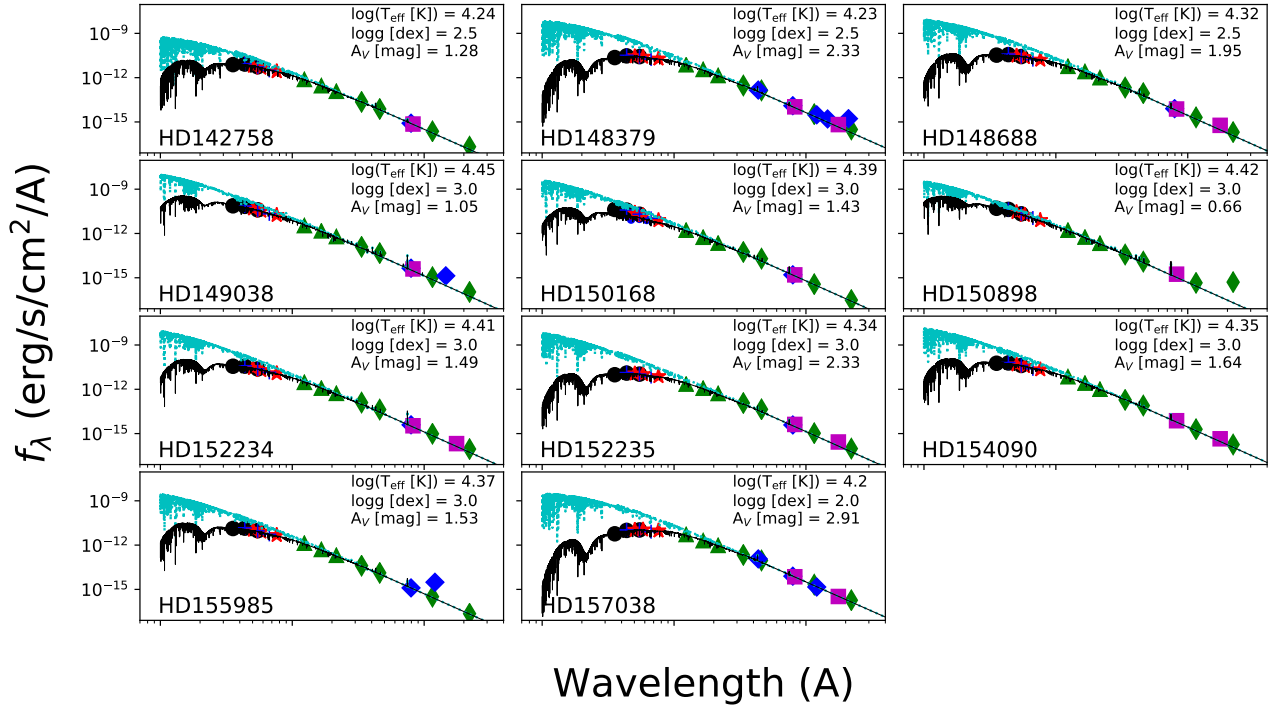


Fig. B.4. Frequency spectra as in Fig. 3, for the stars 31 – 41 from Table A.1.



**Fig. B.5.** Spectral energy distributions and their fitting models as in Fig. 4, for the stars 1 – 30 from Table A.1.



**Fig. B.6.** Spectral energy distributions and their fitting models as in Fig. 4, for the stars 31 – 41 from Table A.1.

### **Appendix C: Independent frequencies**

Independent frequencies of the studied BSGs that were extracted via the iterative pre-whitening process. The resolution of the process over the different windows (consisting of single or stitched consecutive sectors) is determined by the Rayleigh criterion. The S/N values are calculated with respect to the adopted model of the SLF variability.



**Table C.1.** Independent frequencies of the studied BSGs that were extracted from the different observing windows.

Star	Sector(s)	$f_i$ [d <sup>-1</sup> ]	$A_i$ [mmag]	S/N
HD51309	33	0.1627	6.3	43
		0.1162	2.7	18
HD51309	6+7	0.0838	5.5	7
HD64760	34+35	0.5846	2.2	3
		0.3178	2.1	3
HD64760	7+8+9	0.4164	4.1	6
		0.3644	2.4	4
		0.4347	1.7	2
HD64760	61+62	0.3868	1.9	3
		0.6236	1.8	3
HD74371	35+36	0.1310	5.6	15
HD74371	61+62	0.2052	4.0	6
		0.2486	3.4	5
HD74371	8+9	0.1377	9.8	51
		0.1181	10.3	53
HD75149	35+36	0.1867	6.4	17
		0.3098	4.1	12
		0.2184	4.3	12
HD75149	8+9	0.1535	6.0	5
		0.2046	5.3	5
HD75149	62	0.1634	10.1	44
		0.1167	6.5	28
HD77581	62	0.2256	34.0	91
		0.1323	18.2	49
HD77581	8+9	0.2203	28.9	55
		0.1535	10.5	20
HD79186	8+9	0.1141	6.2	11
		0.1653	6.6	12
HD79186	62+63	0.1809	4.1	7
		0.3079	4.2	8
HD79186	35+36	0.1668	7.8	11
		0.2105	7.9	11
HD80558	35+36	0.1412	11.1	20
		0.1177	6.5	11
HD80558	62+63	0.0991	7.6	25
		0.1640	4.9	16
HD80558	9+10	0.0994	5.5	17
		0.1759	3.5	12
HD83183	62+63+64	0.0788	1.2	4
HD83183	36	0.3684	0.8	3
		0.4666	0.7	3
HD83183	10	0.4676	0.6	4
		0.3804	0.5	3
HD91619	63+64	0.1267	6.0	57
		0.0969	4.7	44
HD91619	36+37	0.1239	14.0	108
		0.0813	8.8	67
HD91619	10	0.1070	17.8	322
		0.1529	7.5	135
HD92964	63+64	0.1342	10.1	46
		0.1118	6.2	28
HD92964	10	0.0994	19.6	85
HD92964	36+37	0.1355	11.8	71
		0.0813	8.9	53
HD93840	9+10	0.1076	5.4	4

Star	Sector(s)	$f_i$ [d <sup>-1</sup> ]	$A_i$ [mmag]	S/N
HD93840	63	0.1056	12.6	7
		0.4675	4.9	3
HD93840	36+37	0.1045	5.2	5
		0.2401	3.7	4
HD94493	63+64	0.1789	3.1	4
		0.3243	2.8	3
HD94493	10+11	0.1324	2.1	3
		0.1103	2.1	3
HD96248	10+11	0.1103	8.9	10
HD96248	63+64	0.1401	7.6	7
		0.1022	5.5	5
HD99857	37+38	0.6837	2.2	4
		0.1803	1.6	3
HD99857	64	0.0966	2.3	2
HD99857	10+11	0.3678	2.0	3
		0.1434	1.8	3
HD99953	64	0.0743	12.3	67
HD99953	37+38	0.1127	11.6	18
		0.0751	8.4	13
HD99953	10+11	0.1045	6.9	11
		0.2555	6.4	10
HD103779	37+38	0.1465	3.4	4
		0.4808	2.5	3
HD103779	10+11	0.0956	3.1	4
HD105071	37+38	0.1014	4.2	23
HD105071	11	0.0962	3.9	14
HD105071	64+65	0.1190	4.8	8
		0.3101	3.3	5
HD106343	37+38	0.1013	8.8	15
HD106343	11	0.2517	9.2	12
		0.2072	6.4	8
HD106343	64+65	0.1910	9.2	4
		0.1513	7.3	3
HD108002	37+38	0.1352	5.5	4
		0.3043	4.9	4
HD108002	11	0.1332	4.6	3
HD109867	64+65	0.3387	6.4	9
		0.2090	6.2	8
HD109867	11	0.1850	7.8	23
		0.1258	6.2	18
HD109867	38	0.1098	11.7	13
HD111558	64	0.1338	6.7	37
		0.2230	5.7	32
HD111558	11+12	0.1035	3.7	9
		0.2571	3.0	7
HD111558	38	0.2324	4.1	20
		0.3674	2.2	10
HD111973	11	0.1058	11.8	52
HD111973	37+38	1.0212	5.3	14
		0.2858	4.8	8
HD111973	64+65	1.0196	4.9	10
		0.2774	4.4	5
		0.2126	3.3	4
HD115842	64	0.1189	7.2	26
HD115842	38	0.2473	11.5	32
		0.4271	8.1	23
HD115842	11	0.1628	16.2	23
HD116084	64	0.1040	7.7	32
HD116084	11	0.2017	9.4	27
		0.2985	6.3	18

Star	Sector(s)	$f_i$ [d <sup>-1</sup> ]	$A_i$ [mmag]	S/N
HD116084	38	0.2398	6.3	18
		0.3072	4.6	13
HD117024	11	0.3183	1.9	5
		0.1850	1.6	4
HD119646	11	0.1850	4.8	5
		0.4441	2.8	3
HD119646	38	0.1350	6.4	12
		0.2099	3.6	7
HD119646	65	0.1078	8.8	10
		0.1724	3.7	4
HD122879	38	0.3297	3.2	4
HD122879	11	0.2739	6.9	4
		0.4811	5.9	3
HD125288	38	0.0750	1.8	25
HD125288	65	0.1083	0.6	3
HD125288	11	0.1258	1.2	10
		0.3183	0.8	7
HD125545	11	0.2072	8.7	12
HD125545	38	0.1125	6.0	4
HD141318	65	0.1578	0.7	6
		0.9037	0.5	5
HD141318	39	0.2863	0.5	2
		0.5297	0.4	2
HD141318	12	0.2506	0.9	11
		0.1790	0.6	8
HD142758	12	0.1508	13.8	38
		0.2585	7.9	21
HD142758	39	0.1648	5.0	8
		0.2795	4.2	6
HD148379	66	0.1131	20.0	64
HD148379	12	0.1637	15.2	49
HD148379	39	0.1003	7.7	42
HD148688	39	0.2435	10.3	27
		0.1790	7.7	19
HD148688	66	0.1212	8.8	20
HD148688	12	0.1637	9.1	36
HD149038	39	0.1074	6.9	8
HD149038	66	0.1778	5.7	7
HD150168	66	0.5172	3.8	4
		0.7919	3.8	5
HD150168	39	0.7878	4.7	10
		0.3724	4.2	8
HD150168	12	0.8294	4.0	9
		0.3659	2.7	6
HD150898	66	0.1286	3.9	6
HD150898	39	0.2434	2.6	3
HD150898	12	0.1850	4.1	5
		0.4264	4.0	5
HD152234	39	0.1577	4.6	10
HD152234	12	0.2277	7.0	4
		0.5285	6.3	3
HD152234	66	0.1055	5.0	13
HD152235	39	0.3509	8.7	42
		0.2722	8.0	39
HD154090	12	0.3740	7.2	5
		0.1671	5.9	4
HD154090	39	0.1010	6.2	18
		0.2524	5.2	15
HD154090	66	0.1127	16.7	32
		0.2897	13.9	26

Star	Sector(s)	$f_i$ [d <sup>-1</sup> ]	$A_i$ [mmag]	S/N
HD155985	12	0.1795	2.9	5
		0.4523	2.0	3
HD155985	39	0.1935	3.7	6
		0.3225	3.4	5
HD157038	39	0.1149	14.0	113
		0.1795	6.2	50
HD157038	66	0.1449	9.3	44